Simulating cosmic metal enrichment by the first galaxies

Pallottini, A.; Ferrara, A.; Gallerani, S.; Salvadori, S.; D'Odorico, V.

Published in:
Monthly Notices of the Royal Astronomical Society

DOI:
10.1093/mnras/stu451

Publication date:
2014

Monthly Notices of the ROYAL ASTRONOMICAL SOCIETY

MNRAS **440,** 2498–2518 (2014) doi:10.1093/mnras/stu451

Simulating cosmic metal enrichment by the first galaxies

A. Pallottini,[1⋆] A. Ferrara,[1,2] S. Gallerani,[1] S. Salvadori[3] and V. D'Odorico[4]

[1]*Scuola Normale Superiore, Piazza dei Cavalieri 7, I-56126 Pisa, Italy*
[2]*Kavli Institute for the Physics and Mathematics of the Universe (Kavli IPMU), The University of Tokyo, 5-1-5 Kashiwanoha, Kashiwa 277-8583, Japan*
[3]*Kapteyn Astronomical Institute, Landleven 12, NL-9747 AD Groningen, the Netherlands*
[4]*INAF/Osservatorio Astronomico di Trieste, Via Tiepolo 11, I-34143 Trieste, Italy*

Accepted 2014 March 5. Received 2014 February 28; in original form 2014 January 13

ABSTRACT

We study cosmic metal enrichment via adaptive mesh refinement hydrodynamical simulations in a (10 Mpc h^{-1})^3 volume following the Population III (PopIII)–PopII transition and for different PopIII initial mass function (IMFs). We have analysed the joint evolution of metal enrichment on galactic and intergalactic scales at $z = 6$ and $z = 4$. Galaxies account for $\lesssim$9 per cent of the baryonic mass; the remaining gas resides in the diffuse phases: (a) *voids*, i.e. regions with extremely low density ($\Delta \leq 1$), (b) the true intergalactic medium (IGM, $1 < \Delta \leq 10$) and (c) the circumgalactic medium (CGM, $10 < \Delta \leq 10^{2.5}$), the interface between the IGM and galaxies. At $z = 6$, a galactic mass–metallicity relation is established. At $z = 4$, galaxies with a stellar mass $M_* \simeq 10^{8.5}$ M$_\odot$ show $\log(\mathrm{O}/H) + 12 = 8.19$, consistent with observations. The total amount of heavy elements rises from $\Omega_Z^{\rm SFH} = 1.52 \times 10^{-6}$ at $z = 6$ to 8.05×10^{-6} at $z = 4$. Metals in galaxies make up to $\simeq$0.89 of such budget at $z = 6$; this fraction increases to $\simeq$0.95 at $z = 4$. At $z = 6$ ($z = 4$), the remaining metals are distributed in CGM/IGM/voids with the following mass fractions: 0.06/0.04/0.01 (0.03/0.02/0.01). Analogously to galaxies, at $z = 4$ a density–metallicity ($\Delta - Z$) relation is in place for the diffuse phases: the IGM/voids have a spatially uniform metallicity, $Z \sim 10^{-3.5}$ Z$_\odot$; in the CGM, Z steeply rises with density up to $\simeq 10^{-2}$ Z$_\odot$. In all diffuse phases, a considerable fraction of metals is in a warm/hot ($T\,\mu^{-1} > 10^{4.5}$ K) state. Due to these physical conditions, C IV absorption line experiments can probe only $\simeq$2 per cent of the total carbon present in the IGM/CGM; however, metal absorption line spectra are very effective tools to study reionization. Finally, the PopIII star formation history is almost insensitive to the chosen PopIII IMF. PopIII stars are preferentially formed in truly pristine ($Z = 0$) gas pockets, well outside polluted regions created by previous star formation episodes.

Key words: methods: numerical – intergalactic medium – galaxies: star formation – cosmology: theory.

1 INTRODUCTION

The intergalactic medium (IGM) has been extensively investigated through the study of the H I Lyα forest (Rauch 1998) and the absorption features due to ionized metal species (e.g. Songaila & Cowie 1996) detected in the spectra of high-redshift quasars (QSO). Observations have probed metal enrichment in different intergalactic environments: damped Lyα absorbers, characterized by column densities $\log N_{\rm H\,I}/{\rm cm}^{-2} \gtrsim 20$ and metallicities $10^{-1.5} \lesssim Z/{\rm Z}_\odot \lesssim 10^{-1}$; Lyman limit ($17 \lesssim \log N_{\rm H\,I}/{\rm cm}^{-2} \lesssim 20$) and Ly$\alpha$ forest ($14 \lesssim \log N_{\rm H\,I}/{\rm cm}^{-2} \lesssim 17$) systems, typically enriched at $10^{-3.5} \lesssim Z/{\rm Z}_\odot \lesssim 10^{-2}$ (Meiksin 2009).

The evolution of the IGM enrichment can be studied by measuring the abundance of ionized species at different cosmic times. For example, the C IV density parameter decreases with redshift from $\Omega_{\rm C\,IV} \simeq 8 \times 10^{-8}$ at $z \simeq 0$ to $\Omega_{\rm C\,IV} \simeq 10^{-8}$ at $z \simeq 2.5$ (e.g. D'Odorico et al. 2010), it is constant up to $\lesssim$5 (e.g. Schaye et al. 2003; Cooksey et al. 2010), and could possibly show sign of a downturn, $\Omega_{\rm C\,IV} \lesssim 0.5 \times 10^{-8}$, for $z \gtrsim 5$ (e.g. Becker, Rauch & Sargent 2009; Ryan-Weber et al. 2009; Simcoe et al. 2011; D'Odorico et al. 2013). Similarly, Si IV displays a flat behaviour for $2.5 \lesssim z \lesssim 5$ (Songaila 2001, 2005).

Metals are produced by stars inside galaxies featuring a cosmic star formation rate density (SFR) $\simeq 10^{-2}$ M$_\odot$ yr^{-1} Mpc^{-3} at $z = 0$, increasing up to one order of magnitude at $z \sim 3$ and decreasing by a factor of $\sim 10^2$ for $3 \lesssim z \lesssim 9$ (Dunlop 2013). IGM is metal polluted by galaxies, whose SFR can be used to infer the total metal density parameter. Pettini (1999) has shown that observations account for $\sim$20 per cent of metals at $z \gtrsim 2$, implying that the missing ones must be locked in a warm–hot ionized phase (e.g. Ferrara, Scannapieco & Bergeron 2005).

⋆ E-mail: andrea.pallottini@sns.it

Galaxies with high ($M_* \gtrsim 10^{11}\,M_\odot$) and low ($M_* \lesssim 10^8\,M_\odot$) stellar mass display different characteristics. The local (Panter et al. 2008) and $z \lesssim 3$ (Maiolino et al. 2008; Mannucci et al. 2010) mass–metallicity (M_*-Z) relation shows an increasing metal abundance with M_* from $\sim 10^4\,M_\odot$ (Kirby et al. 2013) up to $\sim 10^{10}\,M_\odot$ and a flattening for higher stellar mass. Similar difference is present in the dark-to-visible mass ratio (e.g. Guo et al. 2010; McGaugh & Wolf 2010; Tolstoy 2010): dwarf galaxies typically show values $\gtrsim 30$, while Milky Way size galaxies have a ratio $\lesssim$15; for increasing mass the value approaches (but does not reach) the cosmological one, $\Omega_m/\Omega_b \sim 6$.

A theoretical framework must auto-consistently account for the history of IGM enrichment, its thermal state and the global evolution of galaxy formation. An attractive scenario consists in the so-called pre-enrichment (Madau, Ferrara & Rees 2001; Ferrara 2008), in which IGM pollution is mainly due to low-mass ($M_* \lesssim 10^7\,M_\odot$) galaxies ejecting metals via supernova (SN) explosions at high redshift ($z \gtrsim 8$). In this picture, massive galaxies are able to retain their metals, thus their evolution follows a closed box chemical model(e.g. Tremonti et al. 2004). On the other hand, low-mass galaxies are prone to material ejection because of the shallower potential well and since their smaller size allows the SN to coherently drive the outflows (e.g. Ferrara & Tolstoy 2000).

Ejection from low-mass galaxies has an obvious advantage in terms of volume filling factor, given the abundance of these sources in Λ cold dark matter (ΛCDM) models[1] (i.e. Press & Schechter 1974). Additionally, an early ($z \gtrsim 5$) IGM pollution allows the shocked and enriched gas to cool down (e.g. Ferrara 2008), which can explain the observed narrowness ($\sim$15 km s^{-1}) of the Doppler width of metal lines (Meiksin 2009).

The *pre-enrichment* scenario is appealing because the same low-mass galaxies which start to pollute the IGM can play an important role in the first stages ($z \gtrsim 8$) of cosmic reionization (e.g. Salvadori et al. 2013). In particular (e.g. Choudhury, Ferrara & Gallerani 2008), low-mass galaxies are the ideal hosts for first metal-free Population III (PopIII) stars, which may possibly be responsible for an early ($z \simeq 7$) reionization (e.g. Gallerani et al. 2008a,b). However, the nature of PopIII stars is still under debate, because of lack of observations. From a theoretical point of view, there is no clear consensus on their formation properties (Bromm, Coppi & Larson 2002; Yoshida et al. 2006; Greif et al. 2012; Hosokawa et al. 2012; Meece, Smith & O'Shea 2013), nor their subsequent evolution (Heger & Woosley 2002; Nomoto et al. 2006).

Thus, understanding the IGM metal enrichment from the first galaxies is fundamental to explain both the formation and the evolution of galaxies and the reionization history (Barkana & Loeb 2001; Ciardi & Ferrara 2005). However, it remains to be assessed the evolution of the temperature and chemical state of the enriched IGM, the imprint that the metal transport has on the formation of new star-forming regions and its role in the transition from PopIII to the successive generation of PopII stars. The steady increase of availability of high-redshift IGM observations (e.g. D'Odorico et al. 2013) and their interpretation can hopefully clarify the picture, by better constraining the theoretical models.

Cosmological numerical simulations have been extensively used to study the problem (Aguirre & Schaye 2007; Johnson 2011). However, the huge dynamical range of the underlying physical phenomena makes a true auto-consistent simulation impossible. A viable modelization can be achieved by using subgrid models. These depend both on the considered physics and code implementation. Recently, Hopkins, Narayanan & Murray (2013) studied the impact of different star formation criteria, Agertz et al. (2012) and Vogelsberger et al. (2013) analysed the effect of including different kind of feedback, and the AQUILA project (i.e. Scannapieco et al. 2012) compared 13 different prescriptions of the mainly used cosmological codes. Subgrid modelling lessens the burden of the large dynamical range, but given the currently available computational capabilities, the numerical resources have to be focused towards either the small or the large scales.

Simulations of small cosmic volumes, i.e. box sizes $\lesssim$ Mpc h^{-1}, concentrate the computational power and allow the usage of highly refined physical models. Greif et al. (2010) studied the transition from PopIII to PopII stars in a $10^8\,M_\odot$ galaxy at $z \sim 10$ assessing the role of radiative feedback; Maio et al. (2010) analysed the same transition by varying several parameters, such as the critical metallicity Z_{crit} that distinguishes the populations, the initial mass function (IMF), the metal yields and the star formation threshold; Xu, Wise & Norman (2013) focalized on pinpointing the remnant of PopIII at high redshift, by employing the same computational scheme of Wise et al. (2012), which analysed the impact of radiation from first stars on metal enrichment at $z \gtrsim 9$; at the same redshift, Biffi & Maio (2013), using an extensive chemical network, studied the properties and the formation of first protogalaxies.

Large-scale ($\gtrsim$5 Mpc h^{-1}) cosmological simulations naturally allow for a fair comparison with the observations. Scannapieco et al. (2006) showed that observation of line-of-sight (l.o.s.) correlations of C IV and Si IV are consistent with a patchy IGM enrichment, confined in metal bubbles of $\sim$2 Mpc h^{-1} at $1.5 \lesssim z \lesssim 3$; by implementing galaxy outflows driven by a wind model, Oppenheimer & Davé (2006) managed to reproduce the flatness of $\Omega_{C\,IV}$ at $2 \lesssim z \lesssim 5$; Tornatore, Ferrara & Schneider (2007) found evidence of PopIII production at $z \gtrsim 4$, hinting at the possibility of observing metal-free stars; using a galactic super wind model, Cen & Chisari (2011) simulated a 50 Mpc h^{-1} box finding, among other results, good agreement with observations for $\Omega_{C\,IV}$ and a reasonable match for Ω_{OVI}; by using a $(37.5\,\mathrm{Mpc}\,h^{-1})^3$ volume simulation evolved up to $z = 1.5$, and considering different IMFs and feedback mechanisms, Tescari et al. (2011) analysed the evolution of $\Omega_{C\,IV}$ and statistics of H I and C IV absorbers at different redshifts; simulating a box with size of 25 Mpc h^{-1} and including various feedback, Vogelsberger et al. (2013) managed to match several observations, as the SFR and stellar mass density (SMD) evolution for $z \lesssim 9$, the galaxy stellar mass function and mass–metallicity relation at $z = 0$.

The aim of this paper is to model the IGM metal enrichment focusing on high redshift ($z \geq 4$) by simulating a volume large enough to include a statistically significant ensemble of galaxies. Clearly, the trade-off consists in a limitation of the resolution and small-scale complexity that can be investigated. Our modelling approach is to limit the number of free parameters of the subgrid prescriptions and constrain them with first galaxies observations, namely both global SFR densities inferred from Ultraviolet (UV) luminosity functions (Bouwens et al. 2012; Zheng et al. 2012) and SMD from stellar energy density fitting (González et al. 2011). This method limits the uncertainty on the feedback prescriptions (e.g. Vogelsberger et al. 2013), and at the same time it allows a large-scale analysis of the metal-enrichment process.

The paper is structured as follows. In Section 2, we describe the numerical implementation of the cosmological simulations whose

[1] In this work, we assume a ΛCDM cosmology with total matter, vacuum and baryonic densities in units of the critical density $\Omega_\Lambda = 0.727$, $\Omega_{dm} = 0.228$, $\Omega_b = 0.045$, Hubble constant $H_0 = 100\,h$ km s^{-1} Mpc^{-1} with $h = 0.704$ and spectral index $n = 0.967$, $\sigma_8 = 0.811$ (Larson et al. 2011).

free parameters are then calibrated by matching SFR and SMD data in Section 3. Sections 4 and 5 contain the analysis of galactic and IGM metal enrichment, respectively. We devote Section 6 to study the effects of varying the PopIII IMF, and in Section 7, we compute and discuss mock QSO absorption spectra, in preparation for a future detailed comparison recent of high-redshift ($4 \lesssim z \lesssim 6$) absorption line data (D'Odorico et al. 2013). Finally, in Section 8, we present our conclusions.

2 COSMOLOGICAL SIMULATIONS

We perform cosmological simulations using a customized version of the publicly available code RAMSES (i.e. Teyssier 2002), which is a fully threaded tree data structure in which the hydrodynamical adaptive mesh refinement (AMR) scheme is coupled with a Particle Mesh (PM3) N-body solver through a Cloud-In-Cell interpolation scheme to compute the Poisson equation.

Our simulation evolves a $10\,h^{-1}$ comoving Mpc box, with 512^3 dark matter (DM) particles. The DM mass unit is $2.06 \times 10^6\,\Omega_{\rm dm}\,h^{-1}\,{\rm M}_\odot$, and the baryon base grid spatial resolution is $19.53\,h^{-1}$ kpc. We allow for four additional refinement levels, with a Lagrangian mass threshold-based criterion. This enables us to reach a maximum resolution of $\Delta x_{\rm min} = 1.22\,h^{-1}$ kpc in the densest regions. The initial conditions are generated at $z = 199$ using GRAFIC (i.e. Bertschinger 2001). The gas is characterized by a mean molecular weight $\mu = 0.59$ and has a primordial BBN composition ($Z = 0$) at the starting point of the simulation. We refer to metallicity as the sum of all the heavy element species without differentiating among them, as instead done, e.g. by Maio et al. (2007). To account for heating and cooling processes RAMSES is coupled with ATON (i.e. Aubert & Teyssier 2008), a moment-based radiative transfer code including metal cooling (i.e. Sutherland & Dopita 1993; Theuns et al. 1998). The code allows the treatment of an external, redshift-dependent UV background (UVB, e.g. Haardt & Madau 1996, 2012) produced by both stars and QSOs. In the simulation, we include the UVB and we neglect the radiation from sources inside the box, as the scale of ionized bubbles becomes rapidly comparable to the size of the simulation box (e.g. Wyithe & Loeb 2004; Zahn et al. 2011) and therefore the derived reionization history could not be considered as reliable anyway. We have however verified that varying the UVB within observational limits[2] only marginally affects the enrichment history.

2.1 Star formation prescription

We adopt the star formation recipe described in Rasera & Teyssier (2006) and Dubois & Teyssier (2008), hereafter DT8, whose main features are recalled below. At each coarse time step, Δt, a collisionless star particle is created in every gas cell of size Δx which has a density ρ exceeding the threshold $\rho_{\rm th} \equiv 0.1\,m_H\,{\rm cm}^{-3}$ (Schaye 2004), where m_H is the proton mass. The mass of the newborn particle is $M_{\rm s} = m_* N$, where[3] $m_* = \rho_{\rm th}(\Delta x_{\rm min})^3$ is the resolution-dependent minimum mass of a star particle, and N is drawn from a Poisson distribution

$$P(N) = \frac{\langle N\rangle}{N!}\exp\left(-\langle N\rangle\right), \tag{1a}$$

of mean $\langle N\rangle$ given by

$$\langle N\rangle = \frac{\rho\,(\Delta x)^3}{m_*}\frac{\Delta t}{t_*}\,; \tag{1b}$$

t_* is the local star formation time-scale and represents the first free parameter of our model. The dynamical properties of the star particle formed are inherited from the spawning cell; if the gas cell metallicity is below (above) the critical metallicity, $Z_{\rm crit} \equiv 10^{-4}\,{\rm Z}_\odot$, we label the particle as belonging to the PopIII (PopII) population. Such distinction is used when determining the metal yield and SN explosion energy (Section 2.2).

This recipe ensures that the local SFR follows a Schmidt–Kennicutt relation (i.e. Schmidt 1959; Kennicutt 1998)

$$\dot\rho_* = \frac{\rho}{t_*}\Theta\left(\rho - \rho_{\rm th}\right), \tag{2}$$

where Θ is the Heaviside function.[4] Hereafter, we define as 'star forming' those cells satisfying the density criterion $\rho > \rho_{\rm th}$. As highlighted in Hopkins et al. (2013), different definitions[5] of star-forming regions result in similar star formation histories, provided that stellar feedback is also included.

2.2 Feedback and enrichment prescriptions

The standard RAMSES feedback prescription takes into account both thermal and momentum-driven feedback, as described in DT8. Momentum-driven feedback related to SN blastwaves is important on the typical scales (∼pc) reached by these structures (Agertz et al. 2012); similar arguments apply to radiative feedback from star-forming regions. Since such small scales are not adequately resolved in our simulations, we decided to only include thermal feedback. Also, we do not include active galactic nucleus feedback, which is thought to regulate the star formation of objects with masses $\gtrsim 10^{12}\,{\rm M}_\odot$ (e.g. Teyssier et al. 2011; Vogelsberger et al. 2013) that are rare or absent in our relatively small box.

Every newly-born star particle of mass $M_{\rm s}$ immediately prompts an SN event. This assumption corresponds to the so-called instantaneous recycling approximation (i.e. Tinsley 1980), in turn consistent with the adopted coarse time step ($\Delta t \sim 10\,{\rm Myr}$). SN explosions damp a thermal energy $E_{\rm sn}$

$$E_{\rm sn} = \eta_{\rm sn}\epsilon_{\rm sn}M_{\rm s}, \tag{3}$$

where $\epsilon_{\rm sn}$ is the total SN energy per stellar mass formed and $\eta_{\rm sn}$ is the coupling efficiency. While $\epsilon_{\rm sn}$ depends only on the stellar population properties, $\eta_{\rm sn}$ depends on the numerical implementation and resolution; in practice, we consider $\eta_{\rm sn}$ as the second free parameter of our model. As noted in Dalla Vecchia & Schaye (2012) (see also e.g. Chiosi, Bertelli & Bressan 1992), considering purely thermal feedback is a good assumption if the gas is able to transform the additional thermal energy into kinetic energy before cooling; this can be mimicked by a sufficiently large coupling efficiency $\eta_{\rm sn} \gtrsim 0.1$.

Every explosion returns a gas mass $R\,M_{\rm s}$ and a metal mass $Y\,M_{\rm s}$, that are then removed from the star particle mass. Following Salvadori, Schneider & Ferrara (2007), Salvadori, Ferrara & Schneider (2008), and differently from DT8, we use metallicity-dependent

[2] We have used a simple analytical form of the UVB (Theuns et al. 1998) and varied its parameters.

[3] Following DT8, we impose that no more than half of a cell mass can be converted into stars, i.e. $M_{\rm s} = \min\left[m_* N, 0.5\,\rho(\Delta x)^3\right]$. This prescription ensures the numerical stability of the code.

[4] Note that the Schmidt–Kennicutt relation is written in terms of the surface density, while equation (2) considers the volume density. Thus, we are implicitly assuming a smoothing scale which makes t_* resolution dependent.

[5] Other definitions generally used to identify star-forming regions are based on temperature or molecular hydrogen fraction thresholds, convergent flows requirement or Jeans instability criterion.

Table 1. Adopted IMF-averaged PopII metal yields and gas return fractions [van den Hoek & Groenewegen (1997) for $0.8 \leq m/\mathrm{M}_\odot \leq 8$ and Woosley & Weaver (1995) for $8 \leq m/\mathrm{M}_\odot \leq 40$; explosion energies (in erg $\mathrm{M}_\odot^{-1}$) are taken from Woosley & Weaver (1995)].

$\log(Z/\mathrm{Z}_\odot)$	Y	R	$\epsilon_{\mathrm{PopII}}$
−4.0	0.0160	0.4680	10^{50}
−2.0	0.0192	0.4705	10^{50}
−1.0	0.0197	0.4799	10^{50}
0.0	0.0253	0.4983	10^{50}

Table 2. Adopted IMF-averaged PopIII metal yields and gas return fractions, and relative explosion energies. Data are taken from van den Hoek & Groenewegen (1997) for $0.8 \leq m/\mathrm{M}_\odot \leq 8$ and Woosley & Weaver (1995) for $8 \leq m/\mathrm{M}_\odot \leq 40$ for SALP, Kobayashi, Tominaga & Nomoto (2011) for FHN and Heger & Woosley (2002) for PISN.

IMF	Y	R	$\epsilon_{\mathrm{PopIII}}/\epsilon_{\mathrm{PopII}}$
SALP	0.0105	0.46	1
FHN	0.0081	0.76	1
PISN	0.1830	0.45	10

return fractions (R) and metal yields (Y)

$$R = \frac{1}{\langle\Phi\rangle}\int_{m_1}^{m_2}(m-w)\,\Phi\,\mathrm{d}m \tag{4a}$$

$$Y = \frac{1}{\langle\Phi\rangle}\int_{m_1}^{m_2} m_Z\,\Phi\,\mathrm{d}m \tag{4b}$$

with

$$\langle\Phi\rangle = \int_{m_1}^{m_2} m\,\Phi\,\mathrm{d}m, \tag{4c}$$

where $w = w(m, Z)$ and $m_Z = m_Z(m, Z)$ are, respectively, the stellar remnant and the metal mass produced by a star of mass m at a given metallicity, and $\Phi = \Phi(m)$ is the IMF. Both the IMF and the integration limits depend on the stellar population (PopIII or PopII) considered.

The adopted PopII (PopIII) metal yields, gas return fractions and explosion energies are shown in Table 1 (Table 2). For PopII stars, we adopt a Larson–Salpeter IMF (i.e. Larson 1998), with[6] $m_1 = 0.1\,\mathrm{M}_\odot$, $m_2 = 100\,\mathrm{M}_\odot$, following Salvadori et al. (2007). The IMF of PopIII stars is very poorly constrained (e.g. Scannapieco, Schneider & Ferrara 2003). Therefore, we consider three different possibilities: (a) the same Larson–Salpeter IMF (referred to as the SALP case) as PopII stars but with R, Y and ϵ_{sn} calculated for $Z = 0$; (b) a δ-function IMF, i.e. $\Phi = \delta(m - m_0)$, with $m_0 = 25\,\mathrm{M}_\odot$ appropriate for faint hypernovae (FHN) (Salvadori & Ferrara 2012); (c) a top-heavy IMF with $m_1 = 100\,\mathrm{M}_\odot$ and $m_2 = 500\,\mathrm{M}_\odot$ allowing for pair-instability SN (PISN) in the mass range $140\,\mathrm{M}_\odot \leq m \leq 260\,\mathrm{M}_\odot$ (Tornatore et al. 2007).

Throughout the paper, we use the SALP case as the fiducial one; Section 6 is devoted to the analysis of different prescriptions IMF.

[6] With respect to a Salpeter IMF, a Larson IMF has an exponential cut below $m = 0.35\,\mathrm{M}_\odot$.

3 COSMIC STAR FORMATION HISTORY

As explained above, our model contains two free parameters, namely the local star formation time, t_*, and the SN coupling efficiency, η_{sn}. These parameters have important effects (i.e. Rasera & Teyssier 2006) on two observable quantities, the cosmic SFR and SMD as a function of redshift. Broadly speaking, t_* variations shift the SFR curve with respect to the horizontal axis (i.e. redshift), while η_{sn} sets the curve slope. Thus, in order to calibrate these unknowns, we require our simulation results to match the observed cosmic SFR (Bouwens et al. 2012; Zheng et al. 2012) and SMD (González et al. 2011).

The evolution of the cosmic SFR and SMD for the best-fitting subgrid model parameters $t_* = 7.5\,\mathrm{Gyr}$ and $\eta_{\mathrm{sn}} = 0.25$ are shown in Fig. 1, where they are also compared to the above-mentioned observations. The simulated SFR reproduces the data quite accurately in the range $4 \leq z \leq 8.5$; the agreement is still good at higher redshift ($9 \leq z \leq 10.5$), where, however, the limited mass resolution of our simulation yields a fluctuating SFR evolution. For the SMD evolution, the agreement is good, although the predicted slope appears slightly steeper than the observed one (dashed red line). However, our predictions lie within 2σ of the data by González et al. (2011). This level of agreement can be considered as satisfactory. In fact, while the SMD is inferred using spectral energy distributions fitting of a flux-limited sample of galaxies, in our work, the SMD is obtained simply by integrating the SFR. Our procedure then includes both stars and their remnants, regardless of the age.

In Fig. 1, we also plot separately the contribution of PopIII stars to both SFR and SMD. The PopIII SFR initially climbs to a level slightly above $10^{-3}\,\mathrm{M}_\odot\ \mathrm{yr}^{-1}\ (\mathrm{Mpc}\ h^{-1})^{-3}$ at $z = 9$ which is sustained until $z \simeq 6$ (which might then represent a sweet spot for experimental searches); beyond this epoch, PopIII star formation is rapidly quenched. PopIII SFR is always subdominant with respect to the PopII one; however, at $z = 9$ the PopIII rate is smaller only by a factor of $\simeq$10. This finding offers new hope for detecting these elusive stars in the near future, and particularly with JWST which is expected to be able to probe PopIII SNe up to $z \simeq 15$ (e.g. de Souza et al. 2013b; Whalen et al. 2013).

Currently, observations of the He II λ1640 emission line, excited by the hard UV spectra of PopIII stars, can be used to infer upper bounds on PopIII star formation. Cassata et al. (2013) estimate an $\mathrm{SFR}_{\mathrm{PopIII}} \lesssim 10^{-6}\,\mathrm{M}_\odot\ \mathrm{yr}^{-1}\mathrm{Mpc}^{-3}$ at $z \simeq 2.5$. While our simulations cannot be carried on beyond $z = 4$ due to the limited volume, the upper limit is well above our simulated curve already at $z = 4$. Cai et al. (2011) used a WFC3/*F*130*N* IR narrowband filter to probe He II λ1640 emission in the galaxy IOK-1 at $z = 6.96$. The detected He II flux $1.2 \pm 1.0 \times 10^{-18}$ erg s^{-1} cm^{-2}, corresponds to a 1σ upper limit on PopIII SFR of 0.5 $\mathrm{M}_\odot\ \mathrm{yr}^{-1}$ in this galaxy (assuming a Salpeter IMF for this population) and representing <6 per cent of the total star formation. If these figures are representative of the cosmic average, they would be in striking agreement with our results that predict at $z = 6.96$, a PopIII to PopII SFR ratio of 7.8 per cent. While this extrapolation to large scales might be unwarranted, the consistency we find might hint at the fact that current experiments are on the verge of tracing the full star formation history of metal-free stars. Resolution effects might affect PopIII SFR; they are discussed in detail in Appendix A.

The overall PopIII evolution is not dissimilar from that found by some previous dedicated studies (Tornatore, Ferrara & Schneider 2007; Wise et al. 2012; Johnson, Dalla & Khochfar 2013); however, we derive a PopIII SFR which is about one order of magnitude higher with respect to the results by Wise et al. (2012) and Johnson

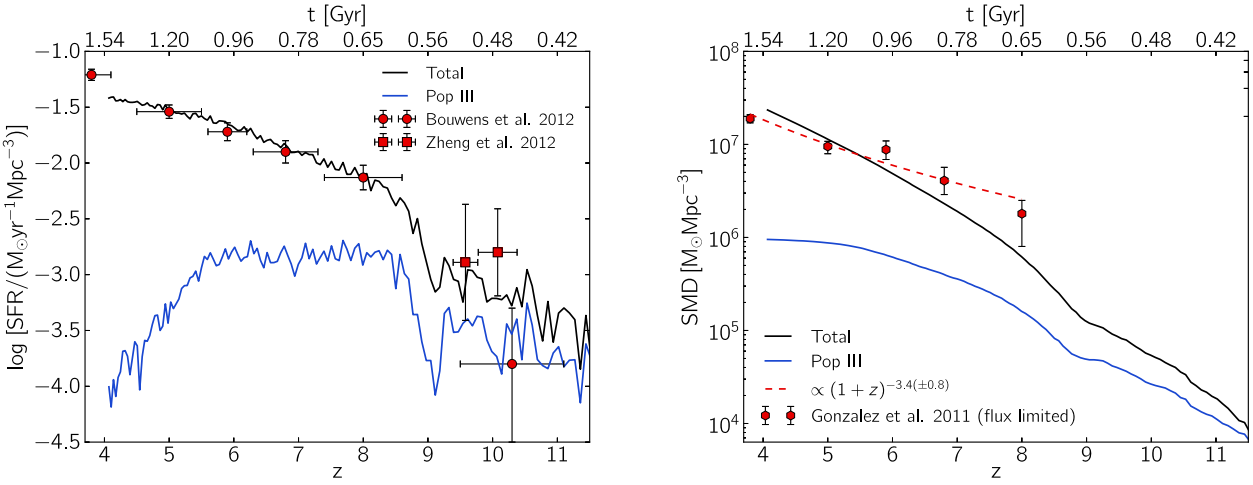

Figure 1. Left-hand panel: cosmic star formation rate density (SFR) as a function of redshift (age of the Universe) for all stellar populations (black line) and for PopIII stars only (blue line). Data points (in red) are taken from Bouwens et al. (2012) and Zheng et al. (2012). Right: cosmic stellar mass density (SMD) as a function of redshift for all stellar populations (black line) and for PopIII stars only (blue line). Data points and the analytical fit (both in red) are from González et al. (2011).

et al. (2013). At present, the source of the discrepancy is unclear as it might be caused by numerical resolution, feedback treatment or limited volume effects. We will come back to this point in Sections 4 and 6.

The first PopIII stars in our simulation start to form in relatively biased regions at $z \simeq 15$. We do not attach a particular significance to this epoch as it is well known that it might depend strongly on the numerical resolution adopted. Earlier studies (e.g. Naoz, Noter & Barkana 2006; Trenti & Stiavelli 2009; Gao et al. 2010; Fialkov et al. 2012; Salvadori et al. 2013) have in fact shown that the first stars in the Universe might form as early as $z \simeq 60$. Instead, it is worth noticing that in the same region after only ∼200 Myr the star formation mode has turned into PopII stars. This shows that even a relatively modest PopIII star formation burst is sufficient to enrich the surrounding gas above $Z_{\rm crit}$, as noted in previous works (e.g. Scannapieco et al. 2003; Salvadori et al. 2008; Greif et al. 2010; Wise et al. 2012) and further elaborated in Section 4.1.

In the following, we focus on the results specifically concerning cosmic metal enrichment. To improve the clarity of the presentation, it is useful to discuss the problem separately for galaxies, the circumgalactic medium (CGM) and the IGM. The exact definitions of these components will be given in Section 5. Albeit this classification might be somewhat arbitrary, there is a clear differentiation among these environments in terms of density and physical processes. We then start by analysing the metal enrichment of galaxies.

4 GALAXIES

We identify galaxies and their hosting halo in each simulation snapshot with the method detailed in Appendix B. In brief, we use a friend-of-friend (FOF) algorithm to identify both DM haloes and the associated star-forming regions; the latter are characterized by the condition that the gas has on overdensity $\Delta \equiv \rho/\langle\rho\rangle > \Delta_{\rm th} \equiv \rho_{\rm th}/\langle\rho\rangle$. We checked that the inferred cumulative halo mass functions are in agreement with the analytical one (Press & Schechter 1974; Sheth & Tormen 1999) to better than 5 per cent at all masses and redshifts. This is about the maximum precision achievable from halo-finder codes (e.g. Knebe et al. 2013).

As expected (Christensen et al. 2010; Wise et al. 2012), stars do not form in haloes resolved with less than $\sim 10^2$ particles, i.e. $M_{\rm h} \simeq 10^{7.5}\,{\rm M}_\odot$. However, physical arguments for star formation suppression in low-mass (mini) haloes have been given in several theoretical (Haiman & Bryan 2006; Alvarez, Finlator & Trenti 2012) and numerical (Wise et al. 2012; Johnson et al. 2013; Xu et al. 2013) works. This happens because, in absence of metals, the dominant gas cooling agent is molecular hydrogen which is easily dissociated by Lyman–Werner (LW) radiation. The mass of the halo determines whether its column density is high enough to self-shield against photodissociation. Hence, for unpolluted minihaloes, PopIII star formation is largely suppressed. Note that the strength of the quenching is still debated (Haiman & Bryan 2006) and in simulations it depends on the specific radiative transfer implementation (Wolcott-Green, Haiman & Bryan 2011).

In our simulation we do not account for the LW background nor do we apply an H_2-based star formation criterion; rather, the quenching of star formation in low-mass haloes is mimicked by mass resolution. This (convenient) numerical feature has also been noted by Xu et al. (2013) in comparison with the previous work of Wise et al. (2012). Xu et al. (2013) have a factor of ∼16 better resolution allowing them to resolve haloes of mass $\sim 10^6\,{\rm M}_\odot$. However, a proper inclusion of the LW background leads Xu et al. (2013) to conclude that the minimum mass of star-forming haloes is $\simeq 3 \times 10^6\,{\rm M}_\odot$, in almost perfect agreement with findings of Wise et al. (2012).

The SFR history is closely connected to the evolution of metal enrichment. The total amount of metals produced by star formation rises from $\Omega_Z^{\rm SFH} = 1.52 \times 10^{-6}$ at $z = 6$ to 8.05×10^{-6} at $z = 4$: this trend follows the growth of the cosmic stellar mass, as $\Omega_Z^{\rm SFH} \propto$ SMD (Ferrara et al. 2005). The metal-enrichment history has been tracked on-the-fly during the simulation. Fig. 2 shows the predicted redshift evolution of the mean metallicity of the gas, $\langle Z\rangle$, calculated by averaging over all the baryons in the simulation volume, and the analogous one for star-forming regions, i.e. $\langle Z\rangle_{\rm SF}$, obtained by averaging only over cells in which $\Delta > \Delta_{\rm th}$.

As we see, $\langle Z\rangle$ monotonically increases with time from $\sim 10^{-6}\,{\rm Z}_\odot$ at $z = 11$ to $\sim 10^{-2}\,{\rm Z}_\odot$ at $z = 4$. This result is consistent with Tornatore et al. (2007), Maio et al. (2010) and Davé, Finlator & Oppenheimer (2011) and expected given the SFR evolution discussed previously.

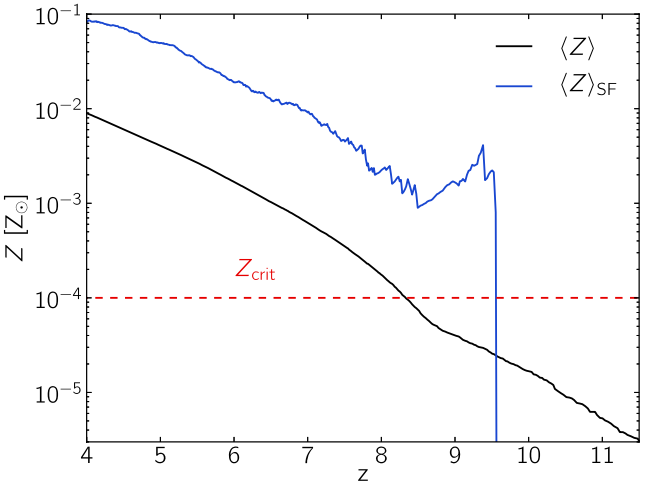

Figure 2. Redshift evolution of the mean metallicity of baryons, $\langle Z \rangle$, (black line) and the mean metallicity of star-forming regions only, $\langle Z \rangle_{SF}$, (blue line). The adopted value, $Z_{crit} = 10^{-4}\,Z_\odot$, of the critical metallicity for the PopIII–PopII transition is indicated with a dashed red line.

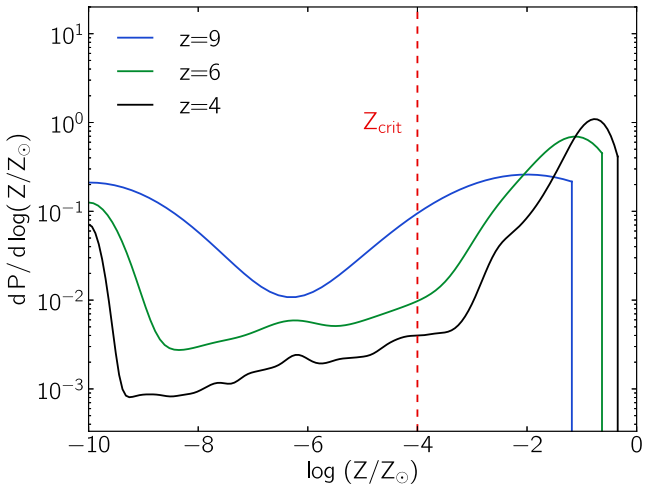

Figure 3. Stellar metallicity distribution function (MDF) at $z = 9$ (blue line), $z = 6$ (green line) and $z = 4$ (black line) for all stars in the simulation box. As in Fig. 2, the critical metallicity $Z_{crit} = 10^{-4}\,Z_\odot$ is indicated with a dashed red line. The amplitude of each curve is normalized so that its integral over the available Z range is equal to 1. Note that for display reasons we have set $Z = 10^{-10}\,Z_\odot$ for stars with $Z < 10^{-10}\,Z_\odot$.

Instead, if we only consider star-forming regions, the mean metallicity evolution of these cells presents a slightly more complex behaviour, also shown in Fig. 2. It raises abruptly from very low values at $z \geq 10$ reaching a peak of $4 \times 10^{-3}\,Z_\odot$ at $z = 9.3$, consistently with the metallicity level obtained by Greif et al. (2010) in the inner part of a galaxy witnessing a single PISN explosion. After a short (100 Myr) decreasing phase, $\langle Z \rangle_{SF}$ begins to increase steadily. At $z \lesssim 8$ star-forming regions are roughly 10 times more metal rich than the mean of all baryons. This peculiar trend is worth a more close scrutiny.

First, the drop of $\langle Z \rangle_{SF}$ for $z \gtrsim 9.5$ is a selection effect introduced by our density-based definition of star-forming cells ($\rho > \rho_{th}$). In the first low-mass galaxies, experiencing their first star formation event, SN feedback is sufficiently strong to completely disperse their gas and decrease the local gas density below ρ_{th}. As at high z, this situation is almost the rule, $\langle Z \rangle_{SF}$ drops precipitously. This also implies that these galaxies are not able to sustain a steady star formation activity: this early flickering star formation mode is also reflected in the SFR evolution discussed in Fig. 1.

It is only when the feedback action becomes less violent and able to gently regulate the star formation activity of individual galaxies that the process stabilizes. This transition eventually occurs around $z \simeq 8$, after a brief (100 Myr) phase in which metals spread from the interstellar medium (ISM) into the CGM and finally into the IGM. During this phase, $\langle Z \rangle_{SF}$ decreases as a result of the increasing primordial gas mass into which metals are distributed. Note that as soon as a steady star formation activity can be sustained, $\langle Z \rangle_{SF} > Z_{crit}$. Thus, PopIII star formation must be confined to external regions of star-forming galaxies or located in the remaining pristine galaxies. We further discuss this point in the next section and in Section 6.

To summarize, the SFR increase occurs when galaxies (on average) enter the regulated star formation regime. The exact redshift of this transition might in principle vary with numerical resolution. Such dependence is analysed in Section 6 and Appendix A.

4.1 Effects on stellar populations

The enrichment history of a given galaxy, among other aspects, affects the evolution of its stellar populations (e.g. PopIII versus PopII) and it is well quantified by the evolution of $P(Z)$, the mass-weighted stellar metallicity distribution function (MDF), shown in Fig. 3 for three selected epochs, $z = 9$, 6, 4 and for all stars in the simulation box. Recall that we are adopting a critical metallicity for the PopIII–PopII transition $Z_{crit} = 10^{-4}\,Z_\odot$. Since in RAMSES, Z is treated as a passively advected scalar field (e.g. Dubois & Teyssier 2007), in the following, we will consider stars with $Z \leq 10^{-10}\,Z_\odot$ as primordial to exclude spurious effects due to diffusion. When calculating MDFs, we consider all stars formed before the selected redshift.

At all redshifts shown, the MDF displays a pronounced double-peak structure. The low metallicity (PopIII) peak is always centred at $Z \simeq 0$, while the PopII peak grows with cosmic time, contemporarily shifting from $\simeq 10^{-2}\,Z_\odot$ at $z = 9$ to $\simeq 10^{-1}\,Z_\odot$ at $z = 4$. This evolutionary trend is induced by the monotonic increase of the mean metallicity of star-forming regions that we report in Fig. 2; as PopII stars dominate the stellar mass for $4 \leq z \lesssim 9$ (see Fig. 1), the peak position closely tracks the value of $\langle Z \rangle_{SF}$ at a given redshift. It has to be emphasized that since the metallicity is mass weighted, the evolution of $\langle Z \rangle_{SF}$ in Fig. 2 is dominated by the most massive star-forming regions.

Interestingly, as time proceeds the MDF develops a characteristic low-metallicity tail which resembles the one derived from observations of metal-poor stars in the Milky Way (e.g. Caffau et al. 2011; Yong, Carney & Friel 2012; Placco et al. 2013) and Local Group dwarfs (e.g. Frebel, Kirby & Simon 2010; Starkenburg et al. 2010). Clearly, the persisting non-detection of $Z \lesssim 10^{-6}\,Z_\odot$ stars in current available stellar samples, supports the idea that PopIII were more massive than today forming stars, as already pointed out in Salvadori et al. (2007). However, whether the local stellar MDF can be considered as universal remains an open problem.

The MDF evolution can be used to characterize the environments in which PopIII stars formed. To this aim, we construct the indicator R_P expressing the ratio between the number of PopIII stars formed in extremely metal-poor (but not pristine; therefore, these sites have already been enriched by a contiguous star formation episode to

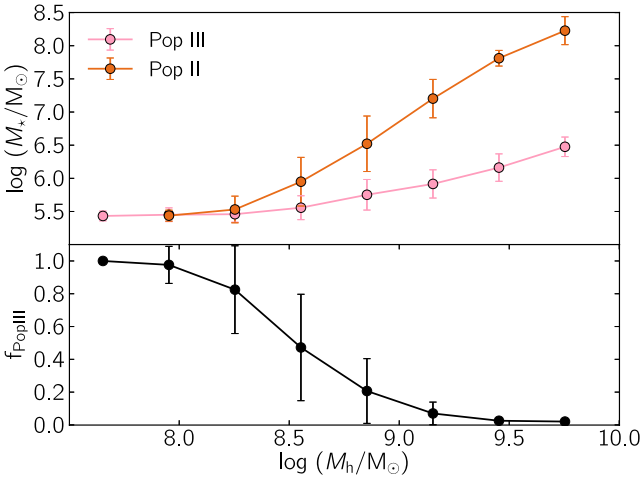

Figure 4. Stellar mass content as a function of the hosting halo mass at $z = 6$. Upper panel: mass in PopII (orange line) and in PopIII (pink line) stars. Lower panel: the fraction of PopIII stars (black line), as defined in the text. The data has been binned in mass (log $M/\,{\rm M}_\odot \simeq 0.3$). Errorbars show the 1σ deviations within the bin.

some $Z_* < Z_{\rm crit}$) environments and the total number of PopIII stars formed:

$$R_P = \frac{1}{N_{\rm III}} \int_{Z_*}^{Z_{\rm crit}} \frac{{\rm d}P}{{\rm d}Z} {\rm d}Z, \tag{5a}$$

where

$$N_{\rm III} = \int_0^{Z_{\rm crit}} \frac{{\rm d}P}{{\rm d}Z} {\rm d}Z. \tag{5b}$$

Assuming $Z_* \equiv 10^{-8}\,{\rm Z}_\odot$, from the previous formula we obtain $R_P(z=9) = 0.29$ and $R_P(z=6) \simeq R_P(z=4) = 0.19$. This result implies that PopIII stars are preferentially formed in purely pristine regions, well outside the polluted regions created by nearby/previous star-forming galaxies. Only a minor fraction of PopIII is formed in inefficiently enriched sites. This scenario is in agreement with the notion of a 'PopIII wave' suggested by Tornatore et al. (2007) and confirmed by Maio et al. (2010), starting from galactic centres and rapidly migrating towards more external regions where pristine gas to sustain their formation can be more easily found. Eventually, the galaxy will run out of unpolluted gas and its PopIII formation comes to a halt.

The $\simeq$1/3 decrease of R_P from $z = 9$ to $z = 6$ indicates that galactic outflows become progressively more efficient in increasing the metallicity of polluted regions above $Z_{\rm crit}$, thus preventing PopIII to form in regions with very low but non-zero metal content. Finally, the negligible R_P variation between $z = 6$ and $z = 4$ is a consequence of the saturation of the PopIII SMD towards $10^6\,{\rm M}_\odot\,{\rm Mpc}^{-3}$ at $z \simeq 5$ (see Fig. 1).

To understand which galaxies are the preferred sites of PopIII star formation, we analyse the $\sim$1600 star-forming haloes at $z = 6$. In the upper panel of Fig. 4, we plot the PopII and PopIII stellar mass ($M_{\rm PopII}$ and $M_{\rm PopIII}$) versus halo mass. We define the PopIII mass fraction as $f_{\rm PopIII} = \langle M_{\rm PopIII}/(M_{\rm PopII} + M_{\rm PopIII})\rangle$, where the average is performed on the mass bin; $f_{\rm PopIII}$ is shown in the lower panel[7] of Fig. 4.

[7] Note that $f_{\rm PopIII} \neq \langle M_{\rm PopIII}\rangle/\langle M_{\rm PopII} + M_{\rm PopIII}\rangle$; not keeping this in mind can lead to misinterpretation when comparing the two panels.

The PopIII mass fraction monotonically decreases with increasing halo mass, going from $\simeq$1 at $M_{\rm h} \sim 10^{7.5}\,{\rm M}_\odot$ to $\lesssim 10^{-2}$ for $M_{\rm h} \gtrsim 10^{9.5}\,{\rm M}_\odot$. This is expected as only small ($M_{\rm h} \lesssim 10^8\,{\rm M}_\odot$) haloes can produce PopIII stars, which are then inherited along the hierarchical formation sequence by larger descendants. The very small scattering in the stellar mass seen in the first two mass bins ($10^{7.5} \lesssim M_{\rm h}/{\rm M}_\odot \lesssim 10^8$) results from the fact that these small haloes have essentially experienced a single (or a few at most) starburst event. As the amount of metals produced is typically sufficient to enrich the gas to values above $Z_{\rm crit}$, the subsequent star formation activity will already produce PopII stars. In conclusion, we suggest that the most suitable halo mass range to observe PopIII stars is $10^{8.4} \lesssim M_{\rm h}/{\rm M}_\odot \lesssim 10^{8.7}$, since in these galaxies PopIII signature can be distinguished from PopII, i.e. $f_{\rm PopIII} \simeq 0.5$, and at the same time their UV luminosities are sufficiently high to be detected in deep JWST spectroscopic surveys around $z = 6$.

4.2 Mass–metallicity relation

Star-forming regions can be identified and associated with their parent galaxy using the technique described in Appendix B. We find a one-to-one match of star-forming regions and galaxies; this is expected, since the finding algorithm does not allow us to resolve substructure on scales $<9.76\,h^{-1}$ kpc. Once the galaxy catalogue at different redshifts has been built, we can relate the gas metallicity of each star-forming region, $Z_{\rm SF}$, with its total (gas+stars) baryonic mass, $M_{\rm SF}$. This relation is shown in Fig. 5 for various redshifts and for a mass bin size log $M/{\rm M}_\odot \simeq 0.2$. The errorbars represent the rms scattering within the mass bin.

At $z = 9$ (blue line), the metallicity is essentially independent of the stellar mass, achieving an almost constant values of $Z_{\rm SF} \simeq 10^{-2.7}\,{\rm Z}_\odot$ in the entire mass range, $10^8 \lesssim M_{\rm SF}/{\rm M}_\odot \lesssim 10^{9.5}$. This surprising behaviour is due to the fact that at $z = 9$ star-forming regions have experienced only one or few bursts. Hence, the $Z_{\rm SF} \simeq 10^{-2.7}\,{\rm Z}_\odot$ enrichment level is set by the dilution of the heavy elements produced by these early bursts into the surrounding ISM. This point can be clarified by the following simple argument. Suppose that a star-forming region has recently formed a mass of stars M_*, and consequently a mass of metals $M_Z = YM_*$. To a first approximation, the surrounding interstellar gas mass swept by the SN

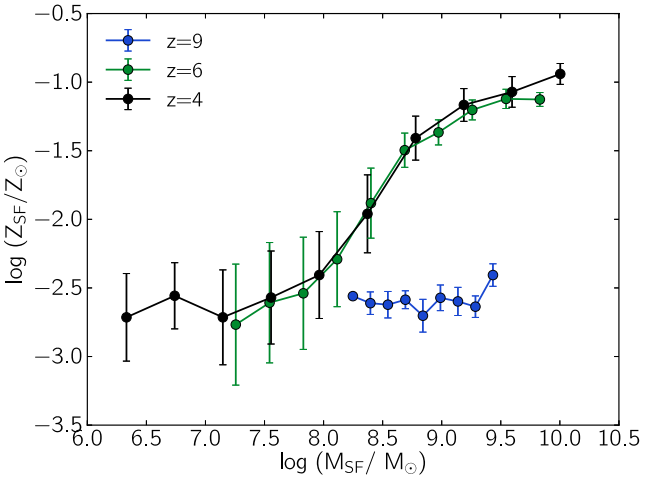

Figure 5. Gas metallicity versus total (gas+stars) baryonic mass in star-forming regions at $z = 9$ (blue line), $z = 6$ (green line) and $z = 4$ (black line). The data have been binned in mass (log $(M/{\rm M}_\odot) \simeq 0.2$). Errorbars show the 1σ deviations within the bin.

blast will be $M_g \propto \epsilon_{\rm sn} M_*$. Hence, the expected gas metallicity from a single burst is $Z_{\rm SF} = M_Z/M_g \equiv$ const., and the mass–metallicity relation shows no trend.

As star formation continues and stabilizes on larger scales, a more definite trend emerges. At $z = 6$ (green line), for example, we see that metallicity increases with stellar mass up to $M_{\rm SF} \simeq 10^{9.2}$, where the relation starts to flatten. This trend becomes slightly more evident at $z = 4$, as it extends to a wider mass range.

On the other hand, for $M_{\rm SF} \gtrsim 10^7\,{\rm M}_\odot$, the shape of the $z = 4$ curve (black line) remains almost identical to $z = 6$, with little signs of evolution over the time span of 600 Myr elapsed between the two epochs, as already pointed out by a recent study by Dayal, Ferrara & Dunlop (2013). Also noticeable is the apparent invariance of the flattening scale, which might be related to the ability of systems with $M_{\rm SF} \gtrsim 10^{9.5}\,{\rm M}_\odot$ to retain most of the produced metals (e.g. Mac Low & Ferrara 1999), in contrast to lower mass systems that are more likely to eject them into the IGM due to their shallower potential wells.

Note that, at $z = 4$, the relation extends below $M_{\rm SF} \lesssim 10^7\,{\rm M}_\odot$: this is due to the presence of satellite galaxies forming in pre-enriched regions of the CGM. Thanks to efficient cooling by metal lines gas in these low-mass systems can now become sufficiently dense to trigger star formation. Similarly to what found at $z = 9$ we see that $M_{\rm SF} \lesssim 10^7\,{\rm M}_\odot$ regions show an almost constant metallicity, $Z_{\rm SF} \sim 10^{-2.7}\,{\rm Z}_\odot$, which is the result of the few bursts of star formation they experienced. Such a flat metallicity trend resembles the one observed in the faintest Local Group dwarf galaxies (e.g. Kirby et al. 2013), and its physical interpretation is in agreement with the findings of Salvadori & Ferrara (2009).

At $z = 4$, we can compare our M_*-Z relation with the observed one, inferred from a sample of 40 galaxies at $3 \lesssim z \lesssim 5$ with masses $10^8\,{\rm M}_\odot \lesssim M_* \lesssim 10^{11}\,{\rm M}_\odot$ (e.g. Troncoso et al. 2013). The simulated high masses ($M_{\rm SF} \gtrsim 10^{9.5}\,{\rm M}_\odot$) star-forming regions contain $M_* \simeq 10^{8.5}$. Averaging their metallicity, we can convert to oxygen abundance by assuming a solar composition (e.g. Asplund et al. 2009): we find $\log({\rm O}/H) + 12 = 8.19$, in agreement within 1σ of the values found by Troncoso et al. (2013).

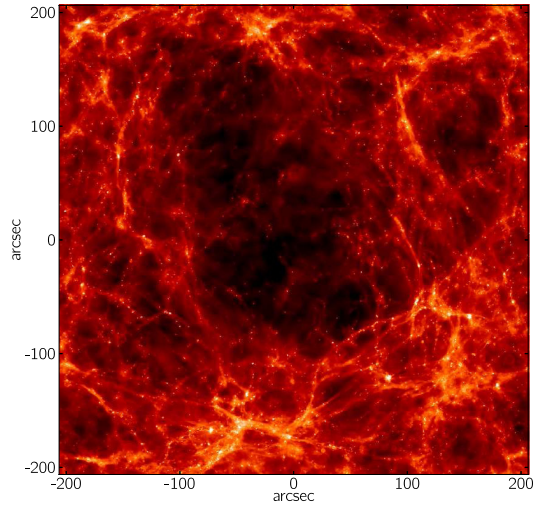

Figure 6. Rendering of the gas temperature and density fields convolution at $z = 4$ for the full 10 Mpc h^{-1} simulation box, corresponding to about 400 arcsec. Details on the rendering technique can be found in Appendix C.

5 DIFFUSE COSMIC GAS

We start by presenting a qualitative overview of the cosmic gas distribution in Fig. 6. The main image shows a rendering of the gas temperature and density fields convolution for the whole simulation box at $z = 4$. The rendering has been obtained using the back-front imaging technique presented in Appendix C. This technique both allows us to clearly identify the typical cosmic web structure made of voids, filaments, knots and clusters, and, thanks to the temperature weighting, the SN shock structures.

More quantitative information can be gathered from the density, temperature and metallicity maps at $z = 4$ (Fig. 7). A comparison between the density and temperature fields allows us to identify both active and/or relic star-forming regions ($\Delta > \Delta_{\rm th}$) that are characterized by shock-heated hot ($T\,\mu^{-1} \gtrsim 10^5$ K) gas contained in approximately spherical bubbles, of size up to several hundred comoving kpc. The hot gas is enriched in heavy elements up to $\simeq 10^{-1}\,{\rm Z}_\odot$ and many of the bubbles can be identified in both maps. However, we see several bubbles with significant metallicity that contain cooler ($2-5 \times 10^4$ K) gas. These bubbles have been produced by earlier stellar populations and had the time to cool via adiabatic

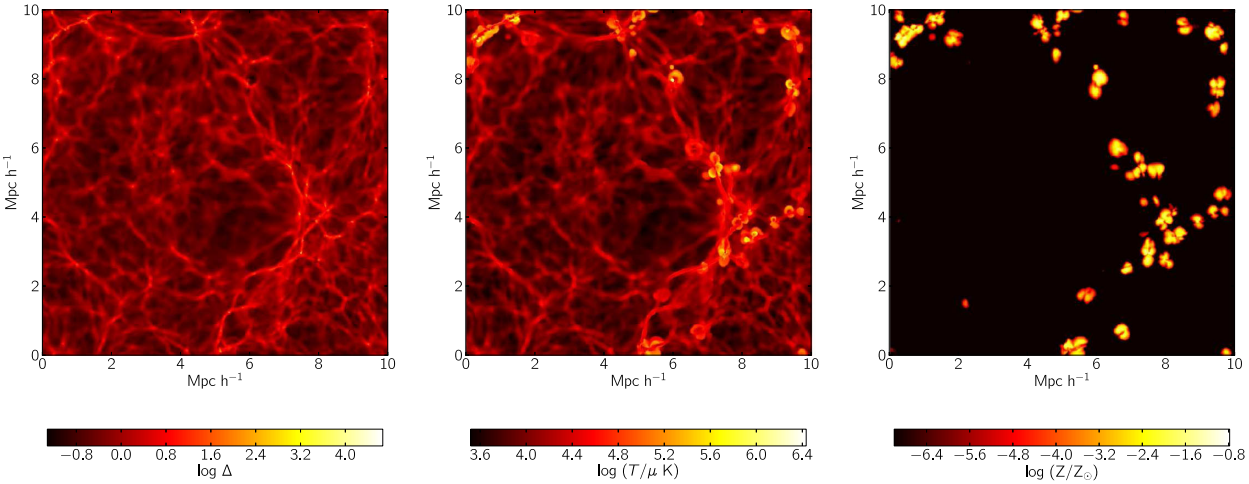

Figure 7. Maps of the simulated gas overdensity, $\Delta = \rho/\langle\rho\rangle$ (left), temperature (centre) and metallicity (right) at $z = 4$ in a slice of thickness 19.53 h^{-1} kpc through the box.

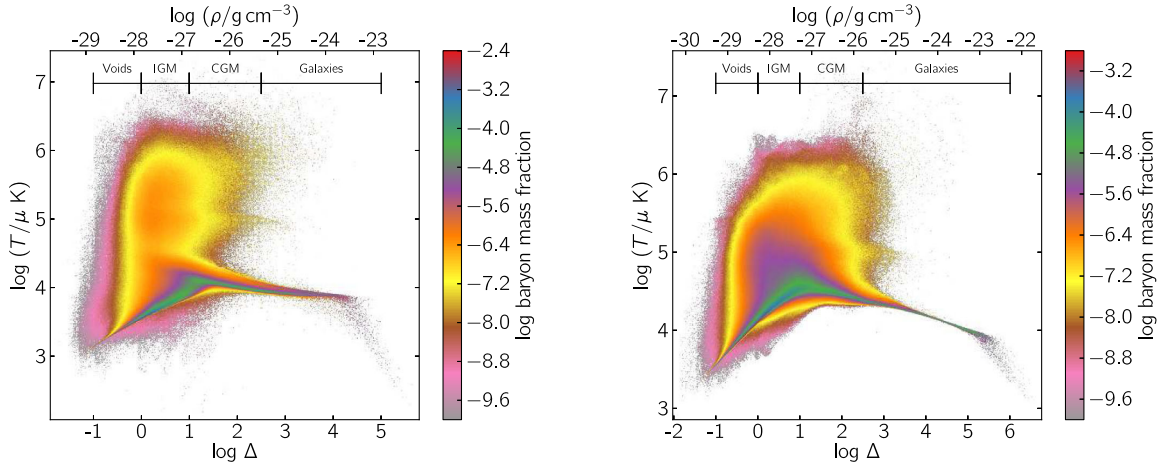

Figure 8. Equation of state (EOS) of the baryons at $z = 6$ (left) and $z = 4$ (right): the colourbar represents the differential mass-weighted probability function. Temperature is expressed in molecular weight units; the density is given both in cgs units and in terms of the overdensity $\Delta = \rho/\langle\rho\rangle$.

expansion and – to a lesser extent – radiative cooling. This implies that metallicity, differently from temperature, retains a fair record of the cosmic star formation activity.

An operative classification of the various cosmic environments can be made in terms of the gas overdensity. In Fig. 8, we show the gas mass-weighted equation of state (EOS) at $z = 6$ and $z = 4$. We can define four different environments: (a) the *voids*, i.e. regions with extremely low density ($\Delta \leq 1$); (b) the true IGM, characterized by $1 < \Delta \leq 10$; (c) the CGM ($10 < \Delta \leq 10^{2.5}$), representing the interface between the IGM and galaxies and (d) high-density ($\Delta > 10^{2.5}$) collapsed structures, that for brevity, we denote as *galaxies*.

This classification does not account for the thermal state of the gas. In fact, all the environments but galaxies are characterized by a range of temperature. For this reason, we will often call 'diffuse phases' the environments (a), (b), (c). As the gas is heated either by photoionization ($T\mu^{-1} \lesssim 10^5$ K) or by shocks ($T\mu^{-1} \gtrsim 10^5$ K), to improve our classification we discriminate between gas colder or hotter than $T\mu^{-1} = 10^5$ K, thus allowing us to readily get an estimate (see Fig. 9) of the relative importance of such heating mechanisms in the various phases.

Fig. 8 allows us to build a complete census of the cosmic baryons. Most of the baryons reside in the diffuse phases, with galaxies accounting only for a tiny fraction of the total mass steadily increasing from $\lesssim$5 per cent at $z = 6$ to $\simeq$9 per cent at $z = 4$. Among diffuse phases, the CGM contains about 15 per cent of the baryons, the remaining fraction being almost equally divided between voids and the IGM with little variation from $z = 6$ to $z = 4$.

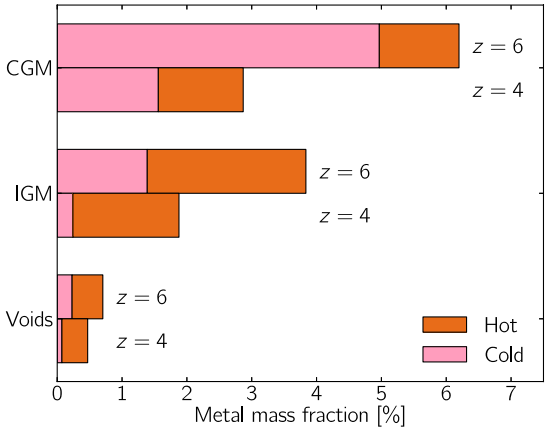

Figure 9. Phase distribution of the *enriched* intergalactic gas at $z = 6$ and $z = 4$. For every phase, the relative cold ($T\mu^{-1} \leq 10^{4.5}$ K) and hot ($T\mu^{-1} > 10^{4.5}$ K) parts are shown in pink and orange, respectively.

At both redshifts, there is a continuous transition from voids to the IGM as both components follow a $T \propto \Delta^{\gamma}$ relation, with an adiabatic index $\gamma = 1/2$. This relation is well known to arise from the balance between adiabatic expansion cooling and photo-heating (e.g. Theuns et al. 1998). In the CGM, however the EOS flattens as a result of the increasing importance of radiative cooling losses, driven both by a higher density and by a larger metal abundance, as we will see in the next section. Metal cooling is important also for the shock-heated IGM. Compared to metal-free simulations (e.g. Pallottini, Ferrara & Evoli 2013), where typical values of the shock-heated gas temperature can reach $T\mu^{-1} \sim 10^8$ K, here metal cooling decreases the bulk temperature of the gas to values $T\mu^{-1} \lesssim 10^6$ K. Overall this picture is consistent with previous results found by Rasera & Teyssier (2006) and also by Cen & Chisari (2011) (in particular see their fig. 20).

5.1 Metal enrichment

Contrary to baryons, which reside predominantly in the IGM, metals are found at any given redshift primarily near their production sites, i.e. in galaxies. However, while at $z = 6$, galactic metals make up to about 90 per cent of the total heavy elements mass, at later epochs ($z = 4$), this fraction increases to 95 per cent as a result of the increased ability of collapsed objects to retain their nucleosynthetic products, thanks to their larger potential wells. Among the diffuse components (see Fig. 9), at $z = 6$, the CGM is more enriched than the IGM (voids) by a factor of 1.6 (8.8), as metals cannot be efficiently transported by winds into distant, low-density regions. Interestingly though, even the most diffuse gas in the voids has been polluted to some extent. We will see later on that by $z = 4$ about 1/10 of the cosmic volume has been enriched to a non-zero metallicity. These results are consistent with previous studies (e.g. Oppenheimer & Davé 2006).

In Fig. 10, we plot the metal mass-weighted EOS at $z = 6$ (left-hand panel) and $z = 4$ (right-hand panel). The temperature structure shows a clear evolution between the two redshifts. The most prominent feature is that the enriched IGM ($\Delta = 1-10$) at $z = 6$ is

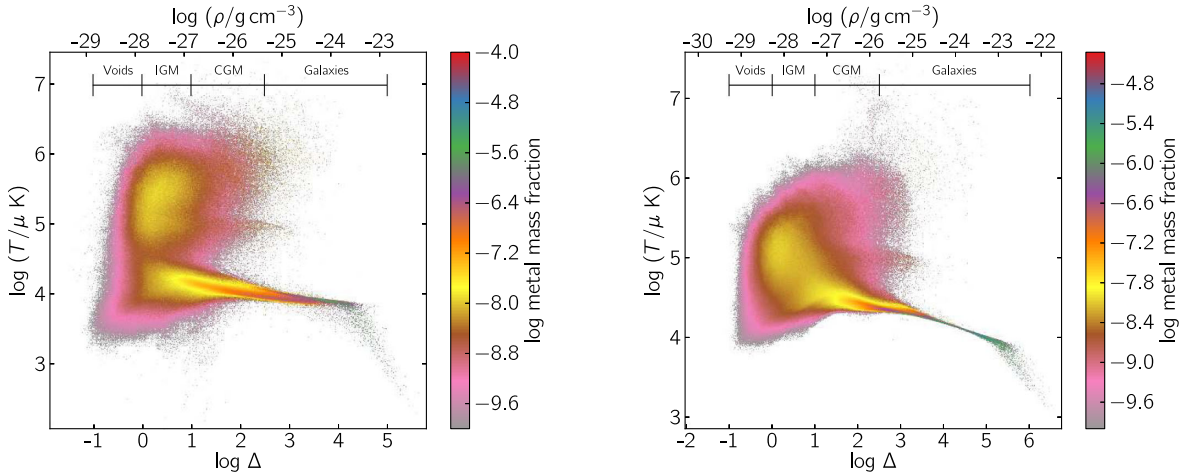

Figure 10. Metal weighted EOS at $z = 6$ (left) and $z = 4$ (right). The notation is the same as in Fig. 8.

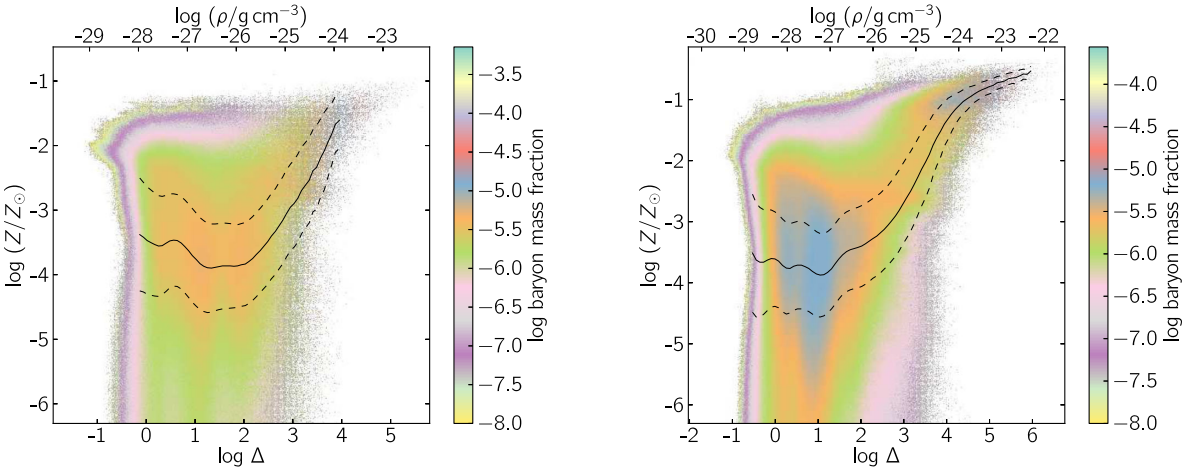

Figure 11. Mass-weighted probability distribution function (PDF) of the baryons at $z = 6$ (left) and $z = 4$ (right) in the metallicity–overdensity plane. The solid (dashed) black line is the mean (rms) metallicity as a function of density.

characterized by a bimodal temperature distribution, which then merges into a single thermal structure by $z = 4$. We interpret this evolution as the result of the early IGM enrichment and heating by winds from low-mass galaxies followed by cooling due to radiative losses. Note that the same temperature feature is visible in the baryonic EOS (Fig. 8). The relative abundance of cold ($T\,\mu^{-1} \leq 10^{4.5}$ K) and hot ($T\,\mu^{-1} > 10^{4.5}$ K) gas in the various diffuse phases is shown in Fig. 9.

The interesting conclusion is that while in the CGM the majority of metals are found to be cold, in the IGM and in voids densities are too low to allow the enriched gas to efficiently cool. Let us then evaluate the cooling time at $z = 6$:

$$t_c(\Delta) = \frac{3}{2}\frac{k_B T}{n\Lambda(T, Z)} \simeq 4.8 \left(\frac{T}{10^6\,\mathrm{K}}\right) \Delta^{-1}\,\mathrm{Gyr}, \quad (6)$$

where we have assumed a value for the cooling function $\Lambda = 2 \times 10^{-23}$ erg cm^3 s^{-1} appropriate for a gas with $T\,\mu^{-1} = 10^6$ K and $Z = 10^{-2}\,\mathrm{Z}_\odot$. Thus, shock-heated, enriched overdensity with $\Delta > 7.6$ will be able to cool during the cosmic time interval between $z = 6$ and $z = 4$, i.e. 0.63 Gyr, consistently with the results of our simulations.

This simple argument also explains the increasing relative fraction of hot metals with decreasing density of the diffuse phases, shown in Fig. 9. This point has two important implications: (a) a considerable fraction of metals are hidden in a hot phase of the CGM/IGM/voids that is difficult to detect via absorption line experiments, highlighting the long-standing missing metals problem already noted by Pettini (1999) and quantified by Ferrara et al. (2005); (b) a small ($\lesssim$1 per cent) but not negligible fraction of metals managed to reach very rarefied environments as the voids, and in some case also to cool. This implies that these metals must have been injected at sufficiently early epochs that they had the time to cool, i.e. as expected in a pre-enrichment scenario (Madau et al. 2001).

The $Z-\Delta$ distribution of the cosmic gas provides additional insights in the metal-enrichment process (Fig. 11). At $z = 6$ (left-hand panel) baryons are nearly uniformly distributed in $10^{-1} \lesssim \Delta \lesssim 10^{2.5}$ and the cosmic gas is characterized by a broad range of metallicities ($10^{-6} \lesssim Z/\mathrm{Z}_\odot \lesssim 10^{-2}$). Besides containing most of the metals, galaxies ($\Delta \gtrsim 10^{2.5}$) show high metallicities ($10^{-2} \lesssim Z/\mathrm{Z}_\odot \lesssim 10^{-1}$) and a loose $Z-\Delta$ correlation. At $z = 4$ (right-hand panel) the distribution evolves and the $Z-\Delta$ correlation at high density becomes tighter and steeper, additionally extending to lower overdensities. Both the IGM and the CGM become preferentially enriched at $10^{-4.5} \lesssim Z/\mathrm{Z}_\odot \lesssim 10^{-2.5}$, i.e. around the critical metallicity for the PopIII transition. The overall shape of the distributions

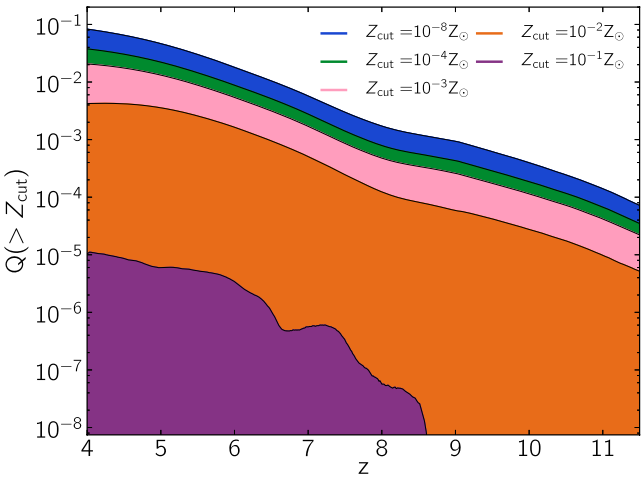

Figure 12. Redshift evolution of the metal volume filling factor, $Q(>Z_{\rm cut})$, for different values of the metallicity cut, $Z_{\rm cut}$. See equation (7) for the definition.

at different z agrees well with those found by Gnedin & Ostriker (1997), Oppenheimer et al. (2012) and with the observed IGM metallicities (e.g. Meiksin 2009).

As time evolves, metals are not only produced at an increasing rate but they are transported by winds away from the production sites. To see this, it is useful to derive the fraction of the cosmic volume, V, filled with heavy elements at a metallicity larger than a given value, $Z_{\rm cut}$. Formally, this can be written as

$$Q(>Z_{\rm cut}) = \frac{1}{V}\int \Theta(Z - Z_{\rm cut})\,{\rm d}V. \quad (7)$$

The behaviour of Q for different values of $Z_{\rm cut}$ has been traced on-the-fly in the simulation. The result is shown in Fig. 12, which highlights interesting features of the enrichment process.

As we have already seen (Fig. 2), the typical metallicity of star-forming regions at $z \simeq 4$ is $\simeq 10^{-1}\,{\rm Z}_\odot$ and corresponds to the lowermost curve in Fig. 12. Even at the lowest redshifts, star-forming regions fill a very small fraction ($\simeq 10^{-5}$) of the volume; however, these sites represent the metal production factories, out of which metals are ejected and distributed by outflows in the CGM and IGM. As a matter of fact, the non-monotonic behaviour at $z \lesssim 6.5$ of $Q(>10^{-1}\,{\rm Z}_\odot)$ is related to the increasing ability of galaxies to retain their metals as they become on average more massive (see Fig. 5).

For lower values of $Z_{\rm cut}$, $Q(>Z_{\rm cut})$ increases rapidly: already the region encompassing a mean metallicity $Z > 10^{-2}\,{\rm Z}_\odot$ fills a volume $\gtrsim 10^3$ times larger (corresponding to a physical scale $\gtrsim 10$ times larger than the star-forming regions). This region corresponds roughly to the CGM, i.e. the transition region surrounding the galaxy that is strongly influenced by the energy and mass input from the latter.

Finally, the $10^{-8} \leq Z_{\rm cut}/{\rm Z}_\odot \leq 10^{-3}$ range corresponds to the IGM (see Fig. 11), where the metal abundance is largely diluted by intergalactic hydrogen. Note that the $Q(>Z_{\rm cut})$ curves for $Z_{\rm cut}$ in the IGM range show little variation, indicating that the IGM metallicity is relatively constant at a value $10^{-3.5}\,{\rm Z}_\odot$. However, only a fraction <10 per cent of the cosmic volume has been ever polluted by heavy elements.

Overall, the filling factor evolution is consistent with the one found by Johnson et al. (2013) for $6 \leq z \lesssim 10$. Additionally, we found an evolution for $10^{-3} \leq Z_{\rm cut}/{\rm Z}_\odot \leq 10^{-2}$ similar to previous works (i.e. Cen, Nagamine & Ostriker 2005; Oppenheimer & Davé 2006; Oppenheimer, Davé & Finlator 2009). However, we find $Q(\geq 10^{-1}\,{\rm Z}_\odot)$ is roughly $\sim$10 times smaller than the corresponding one quoted in Oppenheimer et al. (2009). This is somehow expected, since high metallicity regions correlate with density peaks (see Fig. 11); therefore such discrepancy likely arises from variations in the feedback prescriptions (e.g. Scannapieco et al. 2012) and intrinsic differences between AMR and smoothed particle hydrodynamics (SPH (e.g. Kim et al. 2013; Power, Read & Hobbs 2013). The filling factor of metals has important implications for the relative evolution of PopIII stars and the local transition to a PopII star formation mode that we will discuss in Section 6.

5.2 The circumgalactic medium

We devote this section to some additional points concerning the CGM. We restrict the analysis to $z = 6$ because of the importance of this epoch for reionization (e.g. Pentericci et al. 2011; Schroeder, Mesinger & Haiman 2013) and because it represents the current limiting redshift for QSO absorption line statistical studies (e.g. D'Odorico et al. 2013). The CGM plays a key role in galaxy evolution as it represents the interface between galaxies and the IGM; moreover, ought to its relatively large overdensity and metallicity, it is more readily observed and may serve as a laboratory to study SN feedback. SN winds carve large, hot, metal enriched bubbles in the CGM surrounding their host galaxies, as it is visually represented in Fig. 7.

It is then natural to ask whether relations exist between the properties of these bubbles and their parent galaxy. To answer this question, we first identify a galaxy and the associated metal bubble with the method described in Appendix B, based on a metallicity threshold criterion, i.e. the gas inside a bubble must have $Z > Z_{\rm th} = 10^{-7}\,{\rm Z}_\odot$. Choosing a different $Z_{\rm th}$ would somewhat change the inferred bubble properties; however, the correlations we are going to discuss are insensitive to normalization constants.

As a first step, we classify metal bubbles on the basis of the number of galaxies present in their interiors: in Fig. 13, we use different symbols to differentiate bubbles according to the number of haloes they contain, i.e. $N_{\rm h} = 1$ (blue circle), $1 < N_{\rm h} \leq 5$ (green triangle) and $N_{\rm h} > 5$ (orange squares). Broadly speaking, one can think of the $N_{\rm h}$ parameter as an indicator of merging activity experienced by the bubble. The detailed definitions of the physical quantities characterizing the bubbles are given in Appendix B.

As we will see in the following, to a first-order metal bubble properties can be very well described by the Sedov–Taylor adiabatic blast solution. It is then useful to recall its functional form:

$$V_{\rm B}(t) = \zeta \left(\frac{E}{\rho_e}\right)^{3/5} t^{6/5}, \quad (8)$$

where $V_{\rm B}$ is the bubble volume, $E = \sum_i^{N_{\rm h}} E_i$ is the total SN energy produced by the $N_{\rm h}$ haloes inside the bubble, ρ_e is the mean density of the environment, t is the bubble age and ζ is a dimensionless factor of the order of unity. In the simplest case, E_i is proportional to the stellar mass formed and hence, for a fixed star formation efficiency (see equation 2), to the baryonic mass of the ith star-forming region, $M_{{\rm SF},i}$. It follows that $E \propto \sum_i^{N_{\rm h}} M_{{\rm SF},i} \propto M_{\rm B}$, having further assumed a universal radial density profile within each bubble. In addition, as the post-shock gas temperature is $T_{\rm B} \propto v_B^2$, where v_B is

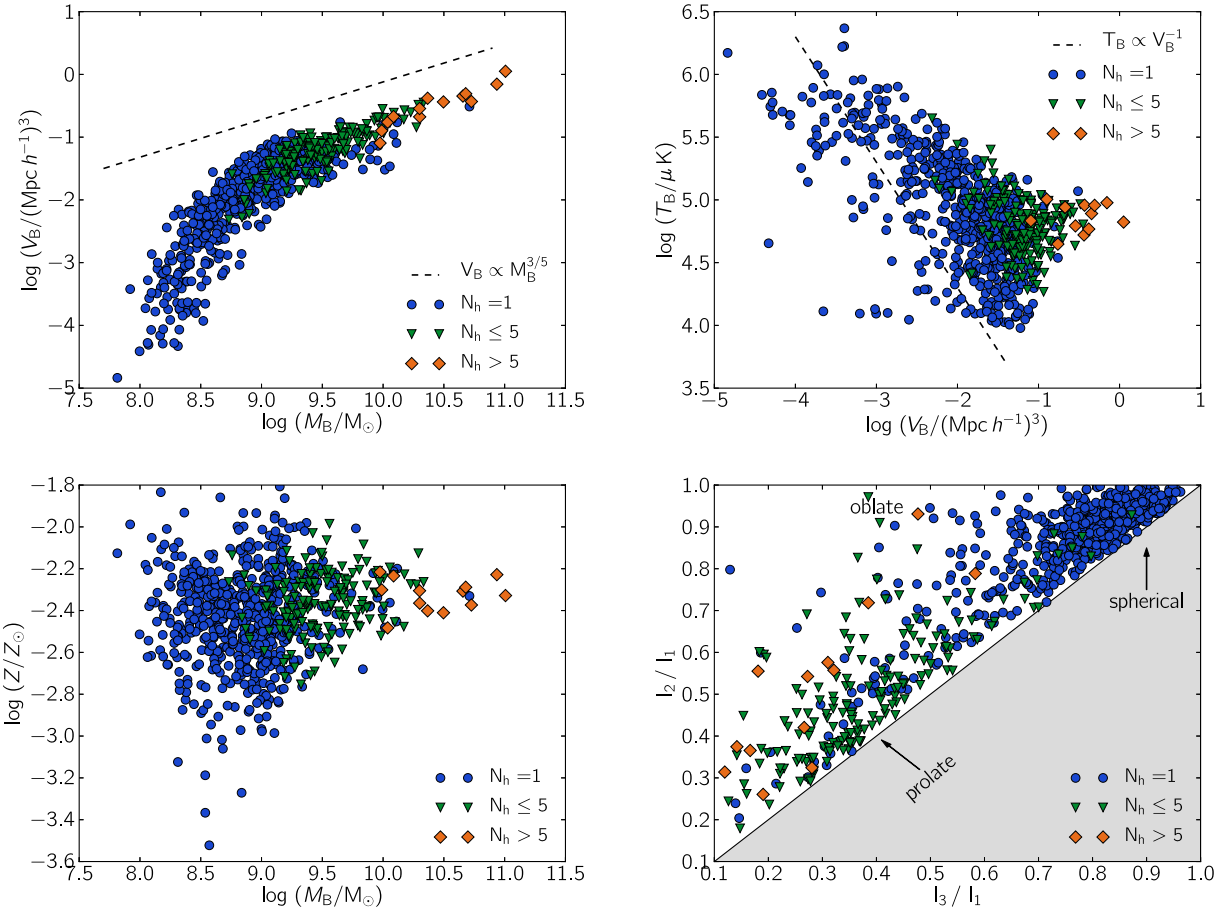

Figure 13. Physical and geometrical properties of metal bubbles at $z = 6$. Upper-left panel: bubble volume versus enclosed gas mass; Upper-right panel: mean bubble temperature versus volume; Lower-left panel: mean bubble metallicity versus enclosed gas mass; Lower-right panel: bubble shape parameters. The number of haloes (N_h) inside the bubble is also indicated. See Appendix B for the details on the definitions. Dashed black lines are the analytical relations inferred from the Sedov–Taylor blast solution (see the text).

the expansion velocity of the bubble, we also find, using equation (8)

$$T_B \propto \left(\frac{E}{\rho_e}\right) V_B^{-1}. \quad (9)$$

We can directly compare the predictions from these simple formulae with the simulation results. The upper-left panel of Fig. 13 shows that the volume of bubbles generally increases with the mass of the galaxies they contain; however, the largest ones result for the coherent action of $\geq$2 galaxies powering them. The $V_B - M_B$ relations follows nicely the $M_B^{3/5}$ analytical form, but smaller bubbles which are still in the initial phases of their evolution deviate from this simple law and have smaller volumes with respect to the mass of the galaxies they contain. The Sedov–Taylor relation accounts well also for the gas temperature within bubbles (upper-right panel) providing a good fit to the slope of singly powered bubbles, while those with $N_h \geq 2$ tend to have hotter bubbles as a result of the larger energy input and replenishment rate of hot gas. Small ($V_B \lesssim 10^{-2}$(Mpc h^{-1})^3) bubbles are typically hotter and reach $T_B\mu^{-1} \gtrsim 10^5$ K. Viceversa, in bubbles with $V_B \sim 10^{-1}$(Mpc h^{-1})^3, the temperatures can be as low as $T_B\mu^{-1} \sim 10^4$ K, i.e. they contain metals that had the time to cool and are currently purely advected with the expansion.

We find no clear correlation between Z and M_B (lower-left panel). This degeneracy mainly depends on the temporal evolution and the geometry. The elapsed time from the last SN explosion characterizes the metallicity spread, as injected metals are diluted into the surrounding medium (Madau et al. 2001). Additionally, the relative outflow-galaxy geometry affects the pollution. As shown by Recchi & Hensler (2013) using 2D chemo-dynamical simulations, the surrounding gas distribution can change the enriched gas metallicity by a factor of $\sim$10. This is particularly relevant at high masses ($M_B \gtrsim 10^9$ M$_\odot$), where the bubbles tend to merge, thus shape effects are dominant. The absence of correlation could have been also expected from the smooth distribution of the CGM/IGM ($\Delta \lesssim 10^{2.5}$) in the $Z-\Delta$ plane (left-hand panel of Fig. 11).

The geometry of the bubbles is influenced by the topology of the cosmic web. The shape of the bubbles can be described in terms of the eigenvalues I_i of the inertia tensor, where $I_1 \geq I_2 \geq I_3$. The ratios of the principal axis are used as index of sphericity (I_3/I_1), prolateness (I_3/I_2) and oblateness (I_2/I_1). The geometry of the bubbles can be analysed in the sphericity–oblateness plane, i.e. I_3/I_1 versus I_2/I_1, shown in the lower-right panel and obtained directly from the actual shape of bubbles in the simulation output. Almost 40 per cent of the bubbles are in the spherically symmetric region ($I_3/I_1 \simeq 1$); most of them ($\sim$90 per cent) correspond to bubble around isolated galaxies. Another $\sim$30 per cent of the bubbles conserves at least a cylindrical symmetry and populates the $I_3/I_1 \simeq I_2/I_1$ diagonal (prolate) and the $I_2/I_1 \simeq 1$ stripe (oblate). These region contains $\sim$70 per cent bubbles which have experienced

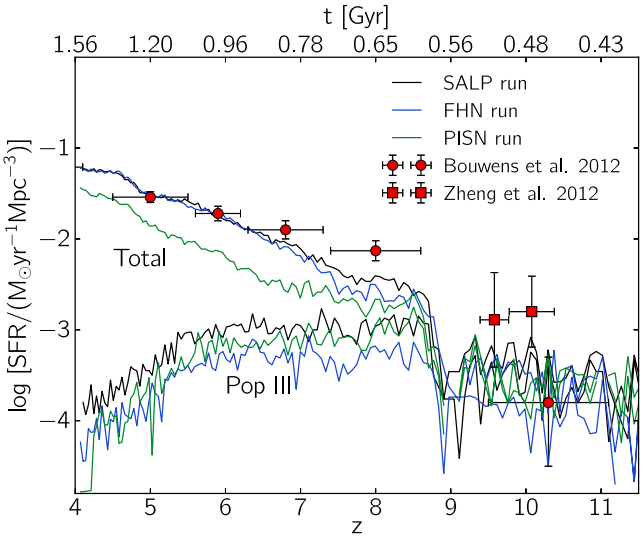

Figure 14. Simulation suite result of cosmic SFRs as a function of redshift (age of the Universe). Different colours correspond to different runs and distinguish the total and PopIII only SFR. See Table 2 for the reference values of the adopted assumptions for the PopIII.

few ($1 < N_{\rm h} \leq 5$) merging events. Because of the elongated shapes, the merging must have occurred along filaments of the cosmic web. The rest (∼35 per cent) have lost any kind of symmetry, and almost all (∼90 per cent) bubbles with large $N_{\rm h}$ values are located in this region. They correspond to metal-polluted bubbles stretching along filaments and linking various knots of the cosmic density field.

6 EFFECTS OF POPIII IMF VARIATIONS

To understand the interplay between cosmic metal enrichment and the PopIII–PopII transition leading to a progressive disappearance of PopIII stars, we have performed an additional set of simulations. The suite is composed of three runs, solely differing in terms of the values adopted for the PopIII stellar parameters (R, Y, $\epsilon_{\rm sn}$), as summarized in Table 2. The single runs are named after the PopIII type selected, i.e. SALP, FHN and PISN.

These simulations, similarly to the fiducial case examined here so far, evolve a 10 Mpc h^{-1} box; however, to limit the computational cost they are made with 256^3 DM particles. Consequently, the mass (spatial) resolution is lower by a factor of 8 (2). The reduced resolution must be compensated with a more efficient star formation, and the best-fitting parameters of the subgrid prescription are now $t_* = 1.5$ Gyr and $\eta_{\rm sn} = 0.3$. Again, the free parameters are fixed by matching the SALP run to the SFR observations (Bouwens et al. 2012) at low ($z \leq 7$) redshift. Note that these parameters are then kept fixed for all the PopIII star choices.

Fig. 14 shows the resulting SFR for the three runs. By comparing with the 512^3 fiducial run presented in Fig. 1, we notice that the lower resolution affects the SFR at $z \gtrsim 8$. However, for the comparison purposes of different PopIII properties this should not represent a major problem, and we also refrain from draw conclusions from $z \gtrsim 8-9$. The lower resolution causes the total SFR to be dominated by PopIII stars up to $z \sim 9$, as feedback is artificially more effective.

Note that there is weak dependence of the redshift at which galaxies become (on average) able to sustain a steady star formation process (see Section 4) on resolution. For the fiducial simulation, this occurs at $z \simeq 8$, while in the rest of the suite it happens at $z \simeq 7.5$. Such epoch roughly coincides with the start of PopIII formation quenching. The two effects are obviously linked as follows from the discussion in the present section.

Let us start by considering the evolution of PopIII SFR. Rather surprisingly, different prescriptions make essentially no differences on PopIII star formation history, apart from a slightly faster drop of PISN SFR below $z = 6$. This more rapid fading can be understood as a result of the $\simeq$10 × higher PISN energy input and metal yield resulting in a more widespread pollution of the volume above $Z_{\rm crit}$. This can be visually appreciated from Fig. 15, featuring metallicity maps at $z = 4$ for the different runs.

Independently of z, the filling factor of regions enriched above the critical metallicity, $Q(>Z_{\rm crit})$, in the PISN run is $\simeq$3 times larger than for the SALP/FHN runs; in addition, the maximum metallicity is about 10 times higher. Based on this evidence, one would expect a much more pronounced suppression of PopIII stars in the PISN case, which however is not observed, apart from the above-mentioned small relative drop at $z < 6$. The results instead point towards a different interpretation. The key point is that enriching to $Z > Z_{\rm crit}$ levels low-density regions in the periphery of galaxies or the CGM does not produce a major effect in the SFR history of PopIII stars because the bulk of active PopIII formation sites is localized in newly forming haloes far from the ones already hosting star formation. This is consistent with the previously discussed outcome of the fiducial run (see Fig. 3 and the corresponding text) that PopIII stars are preferentially formed in a metal-free (rather than with $Z \neq 0$ but below $Z_{\rm crit}$) environment; using semi-analytic models, Crosby et al. (2013) showed that for $z \lesssim 10$, PopIII formation takes place in pristine regions separated by sufficiently large distances.

To better substantiate the last statement, we point out that the PopIII quenching strength is related to the ratio between the typical size of metal bubbles, $\langle R_{\rm B} \rangle = \langle V_{\rm B}^{1/3} \rangle$ (see Section 5.1 and Appendix B), and $r_{\rm SF}$, the correlation length of star-forming regions.[8] In our simulations, we find that $r_{\rm SF} \simeq 2\,{\rm Mpc}\,h^{-1}$ at both $z = 6$ and $z = 4$. At the same time, the mean size of the bubbles goes from $\langle R_{\rm B} \rangle \simeq 0.3\,{\rm Mpc}\,h^{-1}$ at $z = 6$ to $\simeq$0.5 Mpc h^{-1} at $z = 4$, thus quenching PopIII star formation. In fact, we can see from Fig. 1 that the fiducial model predicts ${\rm SFR}_{\rm PopIII}(z = 6) \simeq 10^{1.3}\,{\rm SFR}_{\rm PopIII}(z = 4)$.

In conclusion, the similar evolutionary trend of a flat PopIII SFR, persisting at a level of about $10^{-3}\,{\rm M}_\odot\,{\rm yr}^{-1}\,{\rm Mpc}^{-3}$, up to $z = 6$ and followed by a rapid drop thereafter, appears to be a solid feature of our model and to be independent of the details of PopIII IMF.

This physical interpretation implies that chemical feedback might be artificially enhanced in simulations when the mean pollution radius $\langle R_{\rm B} \rangle$ becomes comparable to the simulation box size. We further discuss how resolution and box-size effects affect this issue in Appendix A. Note that additional uncertainties might come from the treatment of radiative feedback. A proper investigation of resolution and box-size effects would require a suite of simulations with increasing box size and fixed resolution and a convergence study with fixed box-size and increasing mass resolution. We defer this study to a future work.

The effects of PopIII IMF variations have instead a larger impact on PopII (and hence total) SFR. From Fig. 14, we see that, as for the PopIII case, the differences between a SALP or FHN IMF are minor: using Fig. 15 they can be quantified by $\langle |\log Z_{\rm FHN}/{\rm Z}_\odot - \log Z_{\rm SALP}/{\rm Z}_\odot| / \log Z_{\rm SALP}/{\rm Z}_\odot \rangle \simeq 0.01$, where the average is

[8] The correlation length is defined as the scale at which the two-point correlation function of star-forming regions $\xi_{\rm SF}(r_{\rm SF}) = 1$ (e.g. Reed et al. 2009).

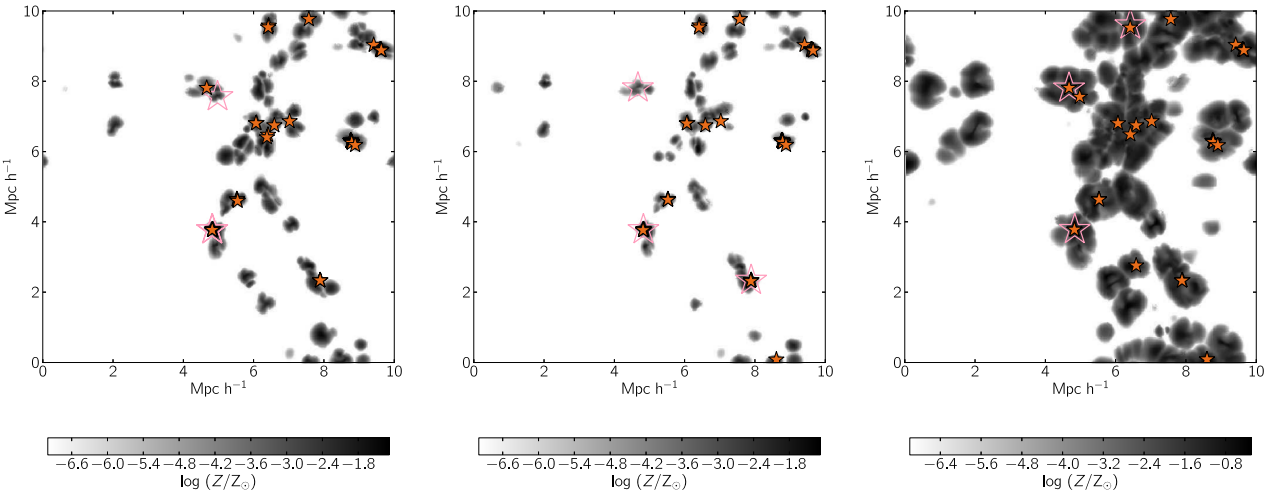

Figure 15. Metallicity maps at $z = 4$ for the SALP (left), FHN (middle), PISN (right) runs. Filled orange small (empty pink large) stars indicate the positions of PopII (PopIII). The slice thickness is $39.06\,h^{-1}$ kpc.

calculated on the slice. This difference is produced by the yields of PopIII SALP versus FHN (Table 2) and from the stochasticity of star formation prescription (equation 1).

On the other hand, differences are noticeable if a PISN IMF is assumed. In this case, the total SFR is depressed by a factor of $\simeq$5 for $z \gtrsim 5$. Because of the higher $\epsilon_{\rm sn}$ value, a pair-instability SN can reach and disrupt a nearby potential star formation site, as also noted by Greif et al. (2010). Instead, less energetic hypernovae or SNe can only pollute their immediate surroundings, failing to reach other more distant and denser environments. Under the assumption of similar local star formation time-scales (t_*) for both PopII and PopIII, the PISN scenario is difficult to be reconciled with the observed global SFR history, as feedback from these stars is probably too effective.

7 SYNTHETIC SPECTRA

We compute mock QSO absorption spectra along several l.o.s. drawn through the simulated box. The details of the adopted technique to compute the H I optical depth are given in Gallerani, Choudhury & Ferrara (2006). Here, we also consider metal absorption lines due to ionic species such as Si IV, C IV, Si II, C II and O I. For these species, we compute the Doppler parameter according to the following expression $b_i = \sqrt{2k_{\rm B}T/m_i}$, where m_i is the mass of the ith species. In Table 3, we report the wavelengths and oscillator strengths (Prochaska et al. 2004) adopted for the considered species.

In order to compute the number density of different ionic species, we have built a grid of model calculations using CLOUDY (Ferland et al. 1998) version 10. We consider a plane parallel slab of gas in pressure equilibrium, illuminated by a Haardt–Madau ionizing background (Haardt & Madau 1996, 2012). The intensity of the ionizing field at 1 Ryd has been normalized so that the photoionization rate, $\Gamma_{\rm H\,I}$ (units: s^{-1}), matches the values predicted by the two reionization models presented in Gallerani et al. (2008a,b), namely an early reionization model (ERM) and a late reionization model (LRM), predicting a reionization redshift of $z_{\rm rei} \simeq 7$ (ERM) and $z_{\rm rei} \simeq 6$ (LRM), respectively.

Table 3. Rest-frame wavelengths λ_i and oscillator strengths f_i (Prochaska et al. 2004) for the transition considered in the simulated QSO spectra with metal absorption lines.

	Si IV	C IV	Si II	C II	O I
λ_i	1393.7550	1548.1950	1526.7066	1334.5323	1302.1685
f_i	0.5280	0.1908	0.127	0.1278	0.0488

We point out that the ionizing background values predicted both by the ERM ($\log\Gamma_{\rm H\,I} = -12.46$) and LRM ($\log\Gamma_{\rm H\,I} = -12.80$) are consistent within 1σ with the measurement of the UVB at $z = 6$ through the flux decrement technique ($\log\Gamma_{\rm H\,I} = -12.74 \pm 0.30$, Wyithe & Bolton 2011); moreover, the ERM (LRM) is consistent within 2.1σ (0.3σ) with the results obtained through the proximity effect technique ($\log\Gamma_{\rm H\,I} = -12.84 \pm 0.18$, Calverley et al. 2011). Each CLOUDY model is characterized by a gas metallicity, density and a constant temperature. As for the chemical composition, we adopt the solar elemental abundance ratios provided in CLOUDY. Calculations are stopped when the depth of the slab reaches our cell resolution.

We interpolate CLOUDY results with the gas properties predicted by the simulation. In Fig. 16, we show the distribution along a random l.o.s. of several quantities, namely: gas density (upper-left panel), peculiar velocity (upper-right panel), gas temperature (lower-left panel) and metallicity (lower-right panel).

Although a detailed, quantitative comparison with observations is beyond the aim of this paper, we include observational artefacts in our simulated spectra, following D'Odorico et al. (2013), a work based on X-shooter spectra. For species with absorption features in the wavelength range $\lambda_i < 1440$ A ($\lambda_i > 1440$ A), since the absorption systems of interest at $z = 6$ are redshifted in the VIS (NIR) region of the X-Shooter spectrum, we smooth the synthetic spectra to a resolution $R = 8800$ ($R = 5600$), we add to each pixel a Gaussian random deviate, yielding a signal-to-noise ratio S/N = 50 (S/N = 10), and we finally re-bin the simulated transmitted flux in channels of width 0.4 A (0.6 A).

An example of the simulated spectra obtained through this procedure is shown in Fig. 17, where the velocity interval corresponds to the redshift range marked through grey hatched regions in Fig. 16. Metal absorption lines show up preferentially in correspondence of metal rich ($Z \gtrsim 10^{-2}\,Z_\odot$), IGM/CGM regions ($\Delta \gtrsim 1 - 10$), characterized by mean temperatures $T\mu^{-1} \simeq 10^{4.5}$ K, as the ones occurring at $z \simeq 5.997$ in our sample l.o.s. As expected, absorption

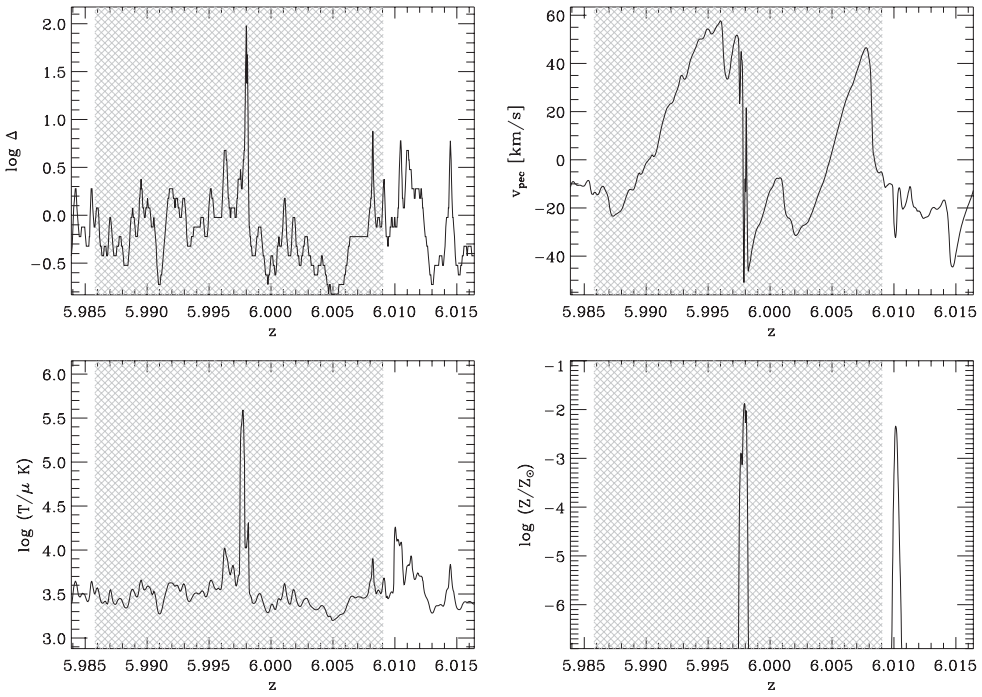

Figure 16. Distribution of the gas density (upper-left panel), peculiar velocity (upper-right panel), temperature (lower-left panel), metallicity (lower-right panel) along a random l.o.s. drawn through the simulated box at $z = 6$.

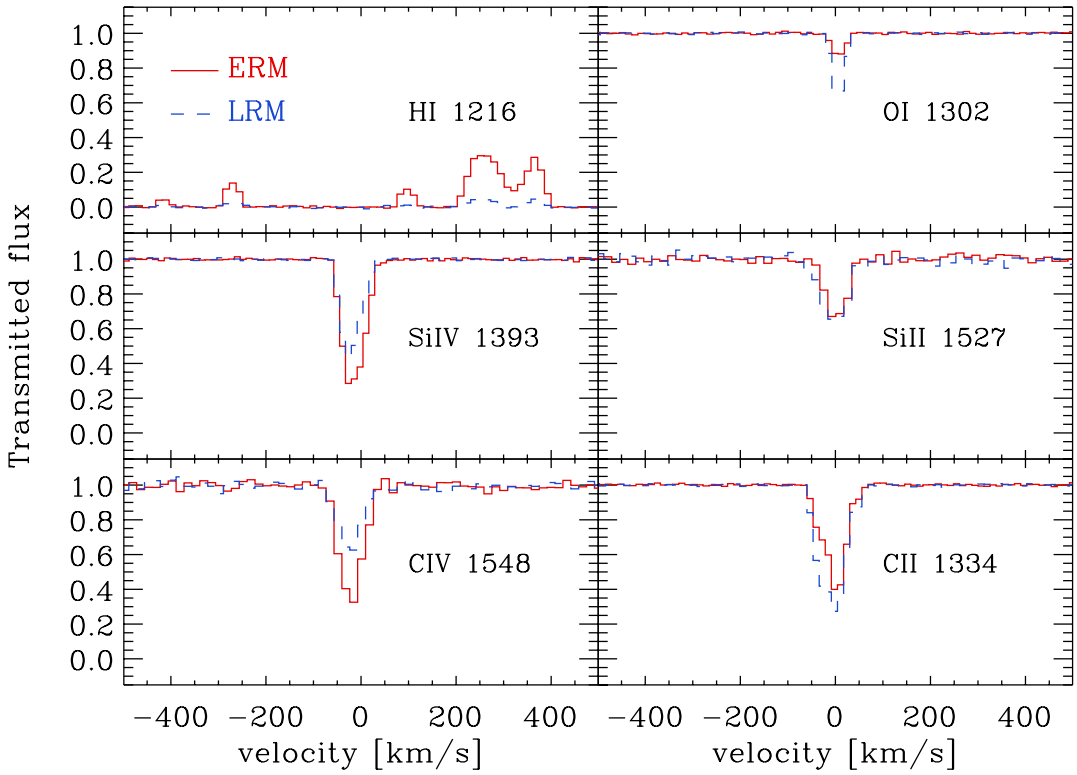

Figure 17. Synthetic spectra extracted from the l.o.s. drawn through the simulated box with physical properties shown in Fig. 16. The spectra are calculated using an early reionization model (ERM, red solid line) and a late reionization model (LRM, blue dashed line) for Lyα forest (upper-left panel) and metal absorption lines (O I, upper-right panel; Si IV and Si II, middle-left and middle-right panel; C IV and C II, lower-left and lower-right panel, respectively). See the text for the definitions.

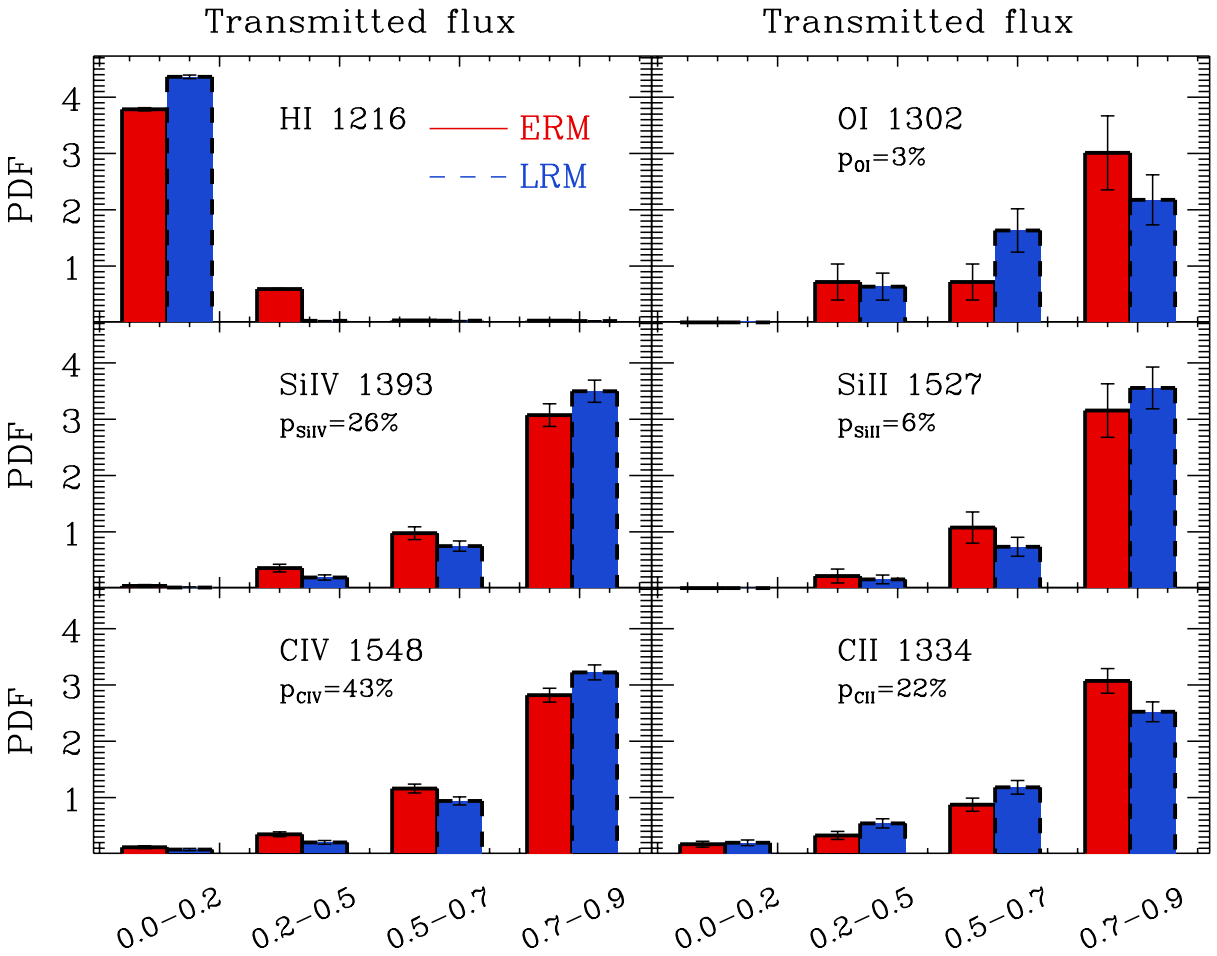

Figure 18. PDFs of the transmitted flux for the species considered in Fig. 17. The solid line (red shaded region) represents our predicted PDF in the case of the ERM, while the dashed line (blue shaded region) denotes LRM results. For each bin, we report the corresponding Poissonian error bars. For each ion, we indicate the probability of encountering its corresponding absorption line in the l.o.s. sample, as defined in the text.

lines due to atoms at high ionization levels (e.g. C IV and Si IV) are more pronounced with respect to low-ionization absorption lines (e.g. Si II and O I) in the case of the ERM, which predicts a higher ionizing background at the redshift of the absorption system. The above relations are reversed in the LRM case.

To get further insight, for each species and reionization model, we compute $N_{\rm los}^{\rm tot} = 300$ synthetic spectra as the ones shown in Fig. 17 and we analyse them in terms of the probability distribution function (PDF) of the transmitted flux ($F_{\rm tr}$). The result is shown in Fig. 18. We divide the transmitted flux in four bins, and for each of them we show the PDF values predicted for the ERM (solid line, red shaded region), LRM (dashed line, blue shaded region), with the corresponding Poissonian error bars. For metal absorption lines, we restrict our analysis to those spectral regions characterized by $F_{\rm tr} < 0.9$. For each species considered, we also report the probability to find at least one absorption line per l.o.s., $p_i = N_{\rm los}^{\rm abs,i}/N_{\rm los}^{\rm tot}$, where $N_{\rm los}^{\rm abs,i}$ is the number of l.o.s. in which we find at least one absorber of the ith species.

Fig. 18 confirms that, in the case of the Lyα forest, the PDF analysis does not provide a fair diagnostics of the IGM ionization level at $z \sim 6$ (Fan, Carilli & Keating 2006; Gallerani et al. 2006; Gallerani et al. 2008a). In fact, from the upper-left panel, it is clear that in both reionization models, most of the pixels are characterized by $F_{\rm tr} \simeq 0.1$, meaning that this statistics is basically dominated by noise.

The same figure shows that, instead, the PDF obtained from metal absorption lines contains a wealth of information, and may provide strong constraints on the ionizing background intensity. It is also interesting to note that the presence of strong O I absorbers ($F_{\rm tr} \simeq 0.3$) does not exclude the possibility that the IGM/CGM is ionized, since these absorption systems are also found in the ERM, which predicts a small neutral hydrogen fraction ($x_{\rm H\,I} \simeq 10^{-4}$) at $z \simeq 6$. Observations of O I absorption systems at these redshifts are useful tools for understanding the metal-enrichment and cosmic reionization processes (Oh 2002; Finlator et al. 2013; Keating et al. 2013).

Finally, as a consistency check, we compute the $\Omega_{\rm C\,IV}$ predicted by our simulation at $z = 6$. The cosmic density parameter relative to the ith species can be written as (e.g. D'Odorico et al. 2013)

$$\Omega_i(z) = \frac{H_0 m_i}{c\rho_{\rm c}} \int N_i\, f_i\, {\rm d}N_i, \qquad (10a)$$

where $\rho_{\rm c}$ is the critical density and $f_i(N_i, z)$ is the PDF of the ith column density N_i. For a discrete set of absorbers indexed by j, the integral can be approximated as (i.e. Storrie-Lombardi, McMahon & Irwin 1996)

$$\Omega_i(z) \simeq \frac{H_0 m_i}{c\rho_{\rm c}} \frac{\sum_j N_i^j}{\Delta X}, \qquad (10b)$$

where ΔX is the cosmological path length of the l.o.s. that can be computed using the following relation:

$$\mathrm{d}X = (1+z)^2 \left(\Omega_\Lambda + \Omega_m (1+z)^3\right)^{-1/2} \mathrm{d}z. \quad (10c)$$

Additionally, the statistical error, $\delta\Omega_i$, is given by

$$\frac{\delta\Omega_i}{\Omega_i} = \frac{\sqrt{\sum_j (N_i^j)^2}}{\sum_j N_i^j}. \quad (10d)$$

Using equations (10), $N_{\rm los}^{\rm tot} = 300$, and taking into account the C IV column density provided by CLOUDY, we find $\Omega_{\rm C\,IV}^{\rm ERM} = (3.8 \pm 0.1) \times 10^{-8}$ and $\Omega_{\rm C\,IV}^{\rm LRM} = (3.1 \pm 0.1) \times 10^{-8}$. We also compute $\Omega_{\rm C\,IV}$, only considering those systems which produce observable absorption lines ($F_{\rm tr} < 0.9$), and which are characterized by $10^{13.4} < N_{\rm C\,IV}/{\rm cm}^{-2} < 10^{15}$. In this case, we find $\Omega_{\rm C\,IV}^{\rm ERM} = (2.9 \pm 0.3) \times 10^{-8}$ and $\Omega_{\rm C\,IV}^{\rm LRM} = (2.3 \pm 0.3) \times 10^{-8}$. Considering the total produced metals ($\Omega_Z^{\rm SFH}$ in Section 4) and assuming solar abundances, it results $\Omega_{\rm C\,IV}/\Omega_{\rm C}^{\rm SFH} \simeq 1.6 \times 10^{-2}$. In other words, we predict that through C IV absorption line experiments it is possible to probe $\simeq$2 per cent of the total carbon present in the IGM/CGM.

We note that the $\Omega_{\rm C\,IV}$ values resulting from our calculations are a factor of $\simeq$3−4 greater than the ones found by D'Odorico et al. (2013). This discrepancy is not surprising, since we are not properly comparing simulations and observations. While our calculations take into account the actual C IV distribution in the simulated box, the observed $\Omega_{\rm C\,IV}$ is inferred from absorption lines spectra through a Voigt profile fitting procedure. Moreover, we restate that our simulations do not account for radiative transfer effects. This is a crucial point, since the ionizing flux which determines the ionization level of atomic species can be dominated by the presence of local sources, rather than the background. In particular, this is relevant for the CGM, which is closer to galaxies and is responsible of strong absorption features.

Constraining the ionization level of the IGM at $z \sim 6$ through metal absorption lines requires both the proper inclusion of radiative transfer effects and an extended statistical analysis (e.g. equivalent width and column density distribution, etc.) of the synthetic spectra. We defer to a future study a comprehensive comparison between observations and absorption spectra extracted from our simulations.

8 CONCLUSIONS

We have studied cosmic metal enrichment via a suite of ΛCDM hydrodynamical simulations using a customized version of the AMR code RAMSES to evolve a (10 Mpc h^{-1})^3 volume up to $z = 4$ with 512^3 DM particles, a corresponding number of coarse grid cells and allowing for four additional levels of refinement. The subgrid prescription for star formation is based on a local density threshold criterion ($\Delta > \Delta_{\rm th}$) and on a critical metallicity criterion ($Z_{\rm crit} = 10^{-4}\,{\rm Z}_\odot$), allowing us to follow the transition from PopIII to PopII stars. To assess the impact of variations in the unknown PopIII IMF, we have investigated three different choices: (a) a standard Larson–Salpeter IMF (SALP), (b) a δ-function describing FHN, and (c) a top-heavy IMF allowing for pair-instability SNe (PISN). We account for thermal feedback from SNe and implemented a metal-dependent parametrization of stellar yields and return fractions.

This set-up enables the resolution of DM haloes masses of $10^{7.5}\,{\rm M}_\odot$ with $\simeq$100 particles and to build a statistically significant sample of galaxies at all redshifts of interest. The two free parameters of our subgrid model (star formation time-scale and SN coupling efficiency) have been fixed by reproducing the observed cosmic SFR (Bouwens et al. 2012; Zheng et al. 2012) and SMD (González et al. 2011) at $4 \leq z \lesssim 10$.

By constructing halo catalogues and identifying the associated stars and star-forming regions ($\Delta > \Delta_{\rm th}$), it has been possible to analyse the evolution of metal enrichment on galactic scales at two representative redshifts, $z = 6$ and $z = 4$. Galaxies account for $\lesssim$9 per cent of the baryonic mass; the complementary fraction resides in the diffuse medium, which we have classified according to the environmental overdensity into: (a) *voids*, i.e. regions with extremely low density ($\Delta \leq 1$), (b) the true IGM ($1 < \Delta \leq 10$) and (c) the CGM ($10 < \Delta \leq 10^{2.5}$), representing the interface between the IGM and galaxies.

We have computed synthetic spectra of metal absorption lines through the simulated box at $z = 6$. The number density of different ionic species are calculated in post-processing with CLOUDY and by considering two physically motivated and observationally constrained reionization models, i.e. an ERM ($\log(\Gamma_{\rm H\,I}/{\rm s}^{-1}) = -12.46$ at $z = 6$) and an LRM ($\log(\Gamma_{\rm H\,I}/{\rm s}^{-1}) = -12.80$).

We have tried to analyse separately the metal-enrichment properties of galaxies and diffuse medium for sake of clarity, but obviously the intimate connection between these two components makes it impossible to separate their description completely. Readers mostly interested in galaxies/stars (diffuse gas) can directly refer to Section 4 (Section 5); those specifically interested in PopIII stars should also find Section 6 relevant. The summary of the main results given below is organized in points attempting to keep these distinctions.

(1) Between $z = 9$ and $z = 6$, a galactic mass–metallicity relation is established. For star-forming regions of mass $M_{\rm SF} \gtrsim 10^7\,{\rm M}_\odot$, such relation shows little evolution from $z = 6$ to $z = 4$. In particular, at $z = 4$, galaxies hosting a stellar mass $M_* \simeq 10^{8.5}\,{\rm M}_\odot$ show a mean oxygen abundance of $\log({\rm O}/H) + 12 = 8.19$, consistent with observations (Troncoso et al. 2013).

(2) At $z = 4$, such relation extends to $M_{\rm SF} \lesssim 10^7\,{\rm M}_\odot$: these are satellite galaxies forming whose star formation has been enabled by the progressive enrichment of the diffuse gas out of which they form. For $10^6 \lesssim M_{\rm SF}/{\rm M}_\odot \lesssim 10^7$, the metallicity trend is flat and resembles the one observed in the faintest Local Group dwarf galaxies (e.g. Kirby et al. 2013).

(3) The total amount of heavy elements produced by star formation rises from $\Omega_Z^{\rm SFH} = 1.52 \times 10^{-6}$ at $z = 6$ to 8.05×10^{-6} at $z = 4$. Metals in galaxies make up to $\simeq$0.89 of such budget at $z = 6$; this fraction increases to $\simeq$0.95 at $z = 4$. At $z = 6$ ($z = 4$), the remaining metals are distributed in the three diffuse phases, CGM/IGM/voids, with the following mass fractions: 0.06/0.04/0.01 (0.03/0.02/0.01).

(4) In all the diffuse phases, a considerable fraction of metals is in a warm/hot ($T\,\mu^{-1} > 10^{4.5}$ K) state. In particular, a small but not negligible mass fraction ($\simeq$0.003) of metals in voids shows $T\,\mu^{-1} \leq 10^{4.5} K$. This implies that these metals must have been injected at sufficiently early epochs that they had the time to cool as expected in a pre-enrichment scenario.

(5) Analogously to the mass–metallicity relation for star-forming regions, at $z = 4$, a density–metallicity ($\Delta - Z$) relation is in place for the diffuse phases. Independently of Δ, the IGM/voids show a uniform distribution around $Z \sim 10^{-3.5}\,{\rm Z}_\odot$, while in the CGM, Z steeply rises with density up to $\simeq 10^{-2}\,{\rm Z}_\odot$.

(6) The geometry of metal bubbles is influenced by the topology of the cosmic web. At $z = 6$, ∼40 per cent are spherically symmetric and are mostly found around isolated galaxies; 30 per cent show

instead a cylindrical shape which mainly results from merging of bubbles aligned along filaments.

(7) The cosmic PopIII star formation history is almost insensitive to the chosen PopIII IMF. PopIII stars are preferentially formed in pockets of pristine ($Z = 0$) gas, well outside polluted regions created by nearby/previous star formation episodes. This supports the 'PopIII wave' scenario suggested by Tornatore et al. (2007) and confirmed by Maio et al. (2010).

(8) In the PISN case, the PopII SFR is suppressed by a factor of $\simeq$5 with respect to the SALP/FHN cases. Because of the higher energy deposition, a PISN can reach and disrupt a nearby potential star formation site, quenching PopII formation. Assuming the same star formation time-scales for PopII and PopIII, a PISN scenario is difficult to be reconciled with the observed SFR history, as the feedback from these stars is probably too effective.

(9) Metal absorption line spectra extracted from our simulations at $z \sim 6$ contain a greater wealth of information with respect to the Lyα forest. Given the prevailing thermodynamical/ionization conditions of the enriched gas, C IV absorption line experiments can only probe up to $\simeq$2 per cent of the total carbon present in the IGM/CGM. However, metal absorption lines are very effective tools to study reionization.

(10) The occurrence of low-ionization metal systems (e.g. O I and C II) in $z \sim 6$ quasar (gamma-ray burst) absorption spectra does not exclude the possibility that the IGM/CGM is on average highly ionized at these epochs. In fact, such systems, although with a lower incidence than in an LRM, are also detectable in the ERM, which predicts a lower H I fraction ($x_{\rm H\,I} \sim 10^{-4}$) at $z \simeq 6$.

In the future, we will perform a more extended statistical analysis of the synthetic spectra, in terms of the equivalent width and column density distributions. This study will enable a direct comparison with recent high-z observations (D'Odorico et al. 2013) and will allow us to constrain cosmic reionization models. Since the ionization level of metal atoms is sensitive to the proximity effect of ionizing sources, it will be crucial to take into account radiative transfer effects. Therefore, we plan to couple our simulation with the new version of the radiative transfer code CRASH3 (Graziani, Maselli & Ciardi 2013). This code allows us to include an arbitrary number of point sources and to reprocess the ionizing radiation through an inhomogeneous distribution of metal-enriched gas, therefore, representing a perfect tool for our planned research.

As a final remark, we have highlighted the potential problem that chemical feedback might be artificially enhanced in a simulation when the box size becomes smaller or comparable to the pollution radius $\langle R_{\rm B} \rangle$. Although the box size and resolution have a significant impact on the determination of PopIII cosmic SFR, additional uncertainties come from the treatment of radiative feedback. A proper demonstration would involve a suite of simulations with increasing box size and fixed resolution and a convergence study with fixed box-size and increasing mass resolution. The situation may be worth a closer scrutiny, which we defer to future work.

ACKNOWLEDGEMENTS

SG thanks INAF for support through an International Post-Doctoral Fellowship. SS acknowledges support from Netherlands Organization for Scientific Research, VENI grant 639.041.233. This work has been partially supported by the PRIN-INAF 2010 grant 'The 1 Billion Year Old Universe: Probing Primordial Galaxies and the Intergalactic Medium at the Edge of Reionization'. RAMSES is governed by the CeCILL license under French law and was written by R. Teyssier, to whom we are very grateful. We thank the anonymous referee for helpful comments.

REFERENCES

Agertz O., Kravtsov A. V., Leitner S. N., Gnedin N. Y., 2012, ApJ, 770, 25
Aguirre A., Schaye J., 2007, in Emsellem E., Wozniak H., Massacrier G., Gonzalez J.-F., Devriendt J., Champavert N., eds, EASP Ser., Vol. 24, How Did the IGM become Enriched? Cambridge Univ. Press, Cambridge, p. 165
Alvarez M. A., Finlator K., Trenti M., 2012, ApJ, 759, L38
Asplund M., Grevesse N., Sauval A. J., Scott P., 2009, ARA&A, 47, 481
Aubert D., Teyssier R., 2008, MNRAS, 387, 295
Barkana R., Loeb A., 2001, Phys. Rep., 349, 125
Becker G. D., Rauch M., Sargent W. L. W., 2009, ApJ, 698, 1010
Bertschinger E., 2001, ApJS, 137, 1
Biffi V., Maio U., 2013, MNRAS, 436, 1621
Bouwens R. J. et al., 2012, ApJ, 754, 83
Bromm V., Coppi P. S., Larson R. B., 2002, ApJ, 564, 23
Caffau E. et al., 2011, A&A, 534, A4
Cai Z. et al., 2011, ApJ, 736, L28
Calverley A. P., Becker G. D., Haehnelt M. G., Bolton J. S., 2011, MNRAS, 412, 2543
Cassata P. et al., 2013, A&A, 556, A68
Cen R., Chisari N. E., 2011, ApJ, 731, 11
Cen R., Nagamine K., Ostriker J. P., 2005, ApJ, 635, 86
Chiosi C., Bertelli G., Bressan A., 1992, ARA&A, 30, 235
Choudhury T. R., Ferrara A., Gallerani S., 2008, MNRAS, 385, L58
Christensen C. R., Quinn T., Stinson G., Bellovary J., Wadsley J., 2010, ApJ, 717, 121
Ciardi B., Ferrara A., 2005, Space Sci. Rev., 116, 625
Cooksey K. L., Thom C., Prochaska J. X., Chen H.-W., 2010, ApJ, 708, 868
Crosby B. D., O'Shea B. W., Smith B. D., Turk M. J., Hahn O., 2013, ApJ, 773, 108
Crow F. C., 1977, Commun. ACM, 20, 799
D'Odorico V., Calura F., Cristiani S., Viel M., 2010, VizieR Online Data Catalog, 740, 12715
D'Odorico V. et al., 2013, MNRAS, 435, 1198
Dalla Vecchia C., Schaye J., 2012, MNRAS, 426, 140
Davé R., Finlator K., Oppenheimer B. D., 2011, MNRAS, 416, 1354
Davis M., Efstathiou G., Frenk C. S., White S. D. M., 1985, ApJ, 292, 371
Dayal P., Ferrara A., Dunlop J. S., 2013, MNRAS, 430, 2891
de Souza R. S., Ciardi B., Maio U., Ferrara A., 2013a, MNRAS, 428, 2109
de Souza R. S., Ishida E. E. O., Johnson J. L., Whalen D. J., Mesinger A., 2013b, MNRAS, 436, 1555
Dolag K., Reinecke M., Gheller C., Imboden S., 2008, New J. Phys., 10, 125006
Dubois Y., Teyssier R., 2007, in Emsellem E., Wozniak H., Massacrier G., Gonzalez J.-F., Devriendt J., Champavert N., eds, EASP Ser., Vol. 24, Metal Enrichment in Galactic Winds. Cambridge Univ. Press, Cambridge, p. 95
Dubois Y., Teyssier R., 2008, A&A, 477, 79 (DT8)
Dunlop J. S., 2013, in Wiklind T., Mobasher B., Bromm V., eds, Astrophysics and Space Science Library, Vol. 396, The First Galaxies. Springer-Verlag, Berlin, p. 223
Fan X., Carilli C. L., Keating B., 2006, ARA&A, 44, 415
Ferland G. J., Korista K. T., Verner D. A., Ferguson J. W., Kingdon J. B., Verner E. M., 1998, PASP, 110, 761
Ferrara A., 2008, in Hunt L. K., Madden S. C., Schneider R., eds, Proc. IAU Symp., 255, Low-Metallicity Star Formation: From the First Stars to Dwarf Galaxies. Kluwer, Dordrecht, p. 86
Ferrara A., Tolstoy E., 2000, MNRAS, 313, 291
Ferrara A., Scannapieco E., Bergeron J., 2005, ApJ, 634, L37
Fialkov A., Barkana R., Tseliakhovich D., Hirata C. M., 2012, MNRAS, 424, 1335
Finlator K., Muñoz J. A., Oppenheimer B. D., Oh S. P., Özel F., Davé R., 2013, MNRAS, 436, 1818

Frebel A., Kirby E. N., Simon J. D., 2010, Nature, 464, 72
Gallerani S., Choudhury T. R., Ferrara A., 2006, MNRAS, 370, 1401
Gallerani S., Ferrara A., Fan X., Choudhury T. R., 2008a, MNRAS, 386, 359
Gallerani S., Salvaterra R., Ferrara A., Choudhury T. R., 2008b, MNRAS, 388, L84
Gao L., Theuns T., Frenk C. S., Jenkins A., Helly J. C., Navarro J., Springel V., White S. D. M., 2010, MNRAS, 403, 1283
Gnedin N. Y., Ostriker J. P., 1997, ApJ, 486, 581
González V., Labbé I., Bouwens R. J., Illingworth G., Franx M., Kriek M., 2011, ApJ, 735, L34
Graziani L., Maselli A., Ciardi B., 2013, MNRAS, 431, 722
Greif T. H., Glover S. C. O., Bromm V., Klessen R. S., 2010, ApJ, 716, 510
Greif T. H., Bromm V., Clark P. C., Glover S. C. O., Smith R. J., Klessen R. S., Yoshida N., Springel V., 2012, MNRAS, 424, 399
Guo Q., White S., 2014, MNRAS, 437, 3228
Guo Q., White S., Li C., Boylan-Kolchin M., 2010, MNRAS, 404, 1111
Haardt F., Madau P., 1996, ApJ, 461, 20
Haardt F., Madau P., 2012, ApJ, 746, 125
Haiman Z., Bryan G. L., 2006, ApJ, 650, 7
Heger A., Woosley S. E., 2002, ApJ, 567, 532
Hopkins P. F., Narayanan D., Murray N., 2013, MNRAS, 432, 2647
Hosokawa T., Yoshida N., Omukai K., Yorke H. W., 2012, ApJ, 760, L37
Johnson J. L., 2011, in Wiklind T., Mobasher B., Bromm V., eds, Astrophysics and Space Science Library, Vol. 396, The First Galaxies. Springer-Verlag, Berlin, p. 177
Johnson J. L., Dalla V. C., Khochfar S., 2013, MNRAS, 428, 1857
Kähler R., Wise J., Abel T., Hege H., 2006, Vol. Graph., 1, 103
Keating L. C., Haehnelt M. G., Becker G. D., Bolton J. S., 2013, MNRAS, 438, 1820
Kennicutt R. C., Jr, 1998, ApJ, 498, 541
Kim J.-h. et al., 2013, ApJS, 210, 14
Kirby E. N., Cohen J. G., Guhathakurta P., Cheng L., Bullock J. S., Gallazzi A., 2013, ApJ, 779, 102
Knebe A. et al., 2013, MNRAS, 435, 1618
Kobayashi C., Tominaga N., Nomoto K., 2011, ApJ, 730, L14
Labadens M., Chapon D., Pomaréde D., Teyssier R., 2012a, in Ballester P., Egret D., Lorente N. P. F., eds, ASP Conf. Ser., Vol. 461, Astronomical Data Analysis Software and Systems XXI., Astron. Soc. Pac., San Francisco, p. 837
Labadens M., Pomarède D., Chapon D., Teyssier R., Bournaud F., Renaud F., Grandjouan N., 2012b, in Pogorelov N. V., Audit E., Zank G. P., eds, Proc 7th Int. Conf., Numerical Modeling of Space Plasma Flows (ASTRONUM2012). Astron. Soc. Pac., San Francisco, p. 287
Larson R. B., 1998, MNRAS, 301, 569
Larson D. et al., 2011, ApJS, 192, 16
Mac Low M.-M., Ferrara A., 1999, ApJ, 513, 142
Madau P., Ferrara A., Rees M. J., 2001, ApJ, 555, 92
Maio U., Dolag K., Ciardi B., Tornatore L., 2007, MNRAS, 379, 963
Maio U., Ciardi B., Dolag K., Tornatore L., Khochfar S., 2010, MNRAS, 407, 1003
Maiolino R. et al., 2008, A&A, 488, 463
Mannucci F., Cresci G., Maiolino R., Marconi A., Gnerucci A., 2010, MNRAS, 408, 2115
McGaugh S. S., Wolf J., 2010, ApJ, 722, 248
Meece G. R., Smith B. D., O'Shea B. W., 2013, ApJ, 783, 75
Meiksin A. A., 2009, Rev. Mod. Phys., 81, 1405
Naoz S., Noter S., Barkana R., 2006, MNRAS, 373, L98
Nomoto K., Tominaga N., Umeda H., Kobayashi C., Maeda K., 2006, Nucl. Phys. A, 777, 424
Oh S. P., 2002, MNRAS, 336, 1021
Oppenheimer B. D., Davé R., 2006, MNRAS, 373, 1265
Oppenheimer B. D., Davé R., Finlator K., 2009, MNRAS, 396, 729
Oppenheimer B. D., Davé R., Katz N., Kollmeier J. A., Weinberg D. H., 2012, MNRAS, 420, 829
Pallottini A., Ferrara A., Evoli C., 2013, MNRAS, 434, 3293
Panter B., Jimenez R., Heavens A. F., Charlot S., 2008, MNRAS, 391, 1117
Pentericci L. et al., 2011, ApJ, 743, 132
Pettini M., 1999, in Walsh J. R., Rosa M. R., eds, Chemical Evolution from Zero to High Redshift. Springer-Verlag, Berlin, p. 233
Placco V. M., Frebel A., Beers T. C., Karakas A. I., Kennedy C. R., Rossi S., Christlieb N., Stancliffe R. J., 2013, ApJ, 770, 104
Power C., Read J. I., Hobbs A., 2013, preprint (arXiv:1307.0668)
Press W. H., Schechter P., 1974, ApJ, 187, 425
Price D. J., 2007, PASA, 24, 159
Prochaska J. X., Chen H.-W., Howk J. C., Weiner B. J., Mulchaey J., 2004, ApJ, 617, 718
Rasera Y., Teyssier R., 2006, A&A, 445, 1
Rauch M., 1998, ARA&A, 36, 267
Recchi S., Hensler G., 2013, A&A, 551, A41
Reed D. S., Bower R., Frenk C. S., Jenkins A., Theuns T., 2009, MNRAS, 394, 624
Ryan-Weber E. V., Pettini M., Madau P., Zych B. J., 2009, MNRAS, 395, 1476
Salvadori S., Ferrara A., 2009, MNRAS, 395, L6
Salvadori S., Ferrara A., 2012, MNRAS, 421, L29
Salvadori S., Schneider R., Ferrara A., 2007, MNRAS, 381, 647
Salvadori S., Ferrara A., Schneider R., 2008, MNRAS, 386, 348
Salvadori S., Tolstoy E., Ferrara A., Zaroubi S., 2013, MNRAS, 437, L26
Scannapieco E., Schneider R., Ferrara A., 2003, ApJ, 589, 35
Scannapieco E., Pichon C., Aracil B., Petitjean P., Thacker R. J., Pogosyan D., Bergeron J., Couchman H. M. P., 2006, MNRAS, 365, 615
Scannapieco C. et al., 2012, MNRAS, 423, 1726
Schaye J., 2004, ApJ, 609, 667
Schaye J., Aguirre A., Kim T.-S., Theuns T., Rauch M., Sargent W. L. W., 2003, ApJ, 596, 768
Schmidt M., 1959, ApJ, 129, 243
Schroeder J., Mesinger A., Haiman Z., 2013, MNRAS, 428, 3058
Sheth R. K., Tormen G., 1999, MNRAS, 308, 119
Simcoe R. A. et al., 2011, ApJ, 743, 21
Songaila A., 2001, ApJ, 561, L153
Songaila A., 2005, AJ, 130, 1996
Songaila A., Cowie L. L., 1996, AJ, 112, 335
Springel V., White S. D. M., Hernquist L., 2004, in Ryder S., Pisano D., Walker M., Freeman K., eds, Proc. IAU Symp. 220, Dark Matter in Galaxies. Astron. Soc. Pac., San Francisco, p. 421
Starkenburg E. et al., 2010, A&A, 513, A34
Storrie-Lombardi L. J., McMahon R. G., Irwin M. J., 1996, MNRAS, 283, L79
Sutherland R. S., Dopita M. A., 1993, ApJS, 88, 253
Tescari E., Viel M., D'Odorico V., Cristiani S., Calura F., Borgani S., Tornatore L., 2011, MNRAS, 411, 826
Teyssier R., 2002, A&A, 385, 337
Teyssier R., Moore B., Martizzi D., Dubois Y., Mayer L., 2011, MNRAS, 414, 195
Theuns T., Leonard A., Efstathiou G., Pearce F. R., Thomas P. A., 1998, MNRAS, 301, 478
Tinsley B. M., 1980, Fundam. Cosm. Phys., 5, 287
Tolstoy E., 2010, in Bruzual G. R., Charlot S., eds, Proc. IAU Symp. 262, Stellar Populations – Planning for the Next Decade. Cambridge Univ. Press, Cambridge, p. 119
Tornatore L., Ferrara A., Schneider R., 2007, MNRAS, 382, 945
Tremonti C. A. et al., 2004, ApJ, 613, 898
Trenti M., Stiavelli M., 2009, ApJ, 694, 879
Troncoso P. et al., 2013, A&A, 563, A58
Turk M. J., Smith B. D., 2011, preprint (arXiv:1112.4482)
van den Hoek L. B., Groenewegen M. A. T., 1997, A&AS, 123, 305
Vogelsberger M., Genel S., Sijacki D., Torrey P., Springel V., Hernquist L., 2013, MNRAS, 436, 3031
Whalen D. J. et al., 2013, ApJ, 777, 110
William E. L., Harvey E. C., 1987, Comput. Graph., 21, 163
Wise J. H., Turk M. J., Norman M. L., Abel T., 2012, ApJ, 745, 50
Wolcott-Green J., Haiman Z., Bryan G. L., 2011, MNRAS, 418, 838
Woosley S. E., Weaver T. A., 1995, ApJS, 101, 181
Wyithe J. S. B., Bolton J. S., 2011, MNRAS, 412, 1926
Wyithe J. S. B., Loeb A., 2004, Nature, 432, 194

Xu H., Wise J. H., Norman M. L., 2013, ApJ, 773, 83
Yong D., Carney B. W., Friel E. D., 2012, AJ, 144, 95
Yoshida N., Omukai K., Hernquist L., Abel T., 2006, ApJ, 652, 6
Zahn O., Mesinger A., McQuinn M., Trac H., Cen R., Hernquist L. E., 2011, MNRAS, 414, 727
Zheng W. et al., 2012, Nature, 489, 406

APPENDIX A: RESOLUTION EFFECTS

As stated in the Introduction, the nature of PopIII stars is still under debate, and there is a lack of consensus on their formation properties and subsequent evolution. Although this paper is not specifically focused on PopIII stars, it is necessary to address numerical effects that could possibly affect PopIII evolution.

Using definitions given in Section 2.1, each PopIII formation event on average spawns a star particle with a mass $M_s = m_*\langle N\rangle$. Using equation (1b), by assuming $\langle N\rangle > 0$ and that one stellar particle is sufficient to pollute its surrounding environment, we can write

$$M_s \propto (\Delta x)^3 \Delta t/t_* \simeq M_{\rm res}^{4/3}/t_*, \tag{A1}$$

where $M_{\rm res}$ is the mass resolution of the AMR simulation, and we have implicitly assumed a Lagrangian mass threshold-based refinement criterion. In equation (A1), M_s is limited from below, since we expect PopIII to form in clouds of mass $\sim 10^2-10^3\,{\rm M}_\odot$ (Bromm et al. 2002; Yoshida et al. 2006; Greif et al. 2012; Hosokawa et al. 2012; Meece et al. 2013); however, for the present estimate, we can neglect this point. Throughout the paper, we have shown that each halo can host at most one PopIII formation event. Assuming no external pollution, an upper limit for the PopIII SFR can be approximated by

$${\rm SFR_{PopIII}} \lesssim M_s n(M > M_h^{\rm min})/t_*, \tag{A2}$$

where $n(M > M_{\rm h}^{\rm min})$ is the number of haloes with mass larger than $M_{\rm h}^{\rm min}$, the minimum mass that can host star formation. For low-mass haloes, we can approximate $n(M > M_{\rm h}^{\rm min}) \sim 1/M_{\rm h}^{\rm min}$ (Press & Schechter 1974; Sheth & Tormen 1999), thus

$${\rm SFR_{PopIII}} \propto \frac{M_{\rm res}^{4/3}}{M_h^{\rm min} t_*^2}. \tag{A3}$$

Numerically, $M_{\rm h}^{\rm min}$ is the mass of haloes resolved by a suitable minimum number of particles, usually taken to be $M_{\rm h}^{\rm min} \simeq 10^{2.5} M_{\rm res}$ (Christensen et al. 2010). From the physical point of view, $M_{\rm h}^{\rm min}$ is determined by feedbacks, star formation criteria and the presence of an LW background (e.g. Wise et al. 2012; Johnson et al. 2013; Xu et al. 2013). Johnson et al. (2013) show that the LW background can induce differences in $\rm SFR_{PopIII}$ up to a factor of $\simeq$8 during the early stages of star formation ($z \gtrsim 10$). Then the scaling provided by equation (A3) reproduces well such result once the proper values of $M_{\rm h}^{\rm min}$ in the Johnson et al. (2013) simulation are inserted for the case with or without LW background.

There is a caveat regarding equation (A3). In our formalism, t_* depends on $M_{\rm res}$, and is calibrated by reproducing the observed SFR/SMD; thus, without a dedicated simulation suite, the $t_*(M_{\rm res})$ functional dependence is uncertain. Moreover, differences in both models and implementations (Scannapieco et al. 2012; Kim et al. 2013) might hinder the effectiveness of the estimate when making a cross-code comparison.

For our fiducial simulation at $z = 6$, the PopIII SFR is $10^{-2.7}\,{\rm M}_\odot\ {\rm yr}^{-1}{\rm Mpc}^{-3}$. Using equation (A3) and considering a slowly varying t_*, our result is compatible with the values reported by Johnson et al. (2013) ($\rm SFR_{PopIII} \simeq 10^{-4}\,M_\odot\ yr^{-1}Mpc^{-3}$) and Wise et al. (2012) ($\rm SFR_{PopIII} \simeq 10^{-4.5}\,M_\odot\ yr^{-1}\,Mpc^{-3}$) at the same redshift.

We remind that we have not taken into account external enrichment. The estimate thus holds up to $z \gtrsim 5$, where in our simulation PopIII star formation is definitively quenched (see Section 4.1). Such quenching redshift is almost independent of resolution (see Section 6).

In principle, the pollution efficiency depends on the ratio between the galaxy correlation length, $r_{\rm SF}$, and the metal bubble size $\langle R_{\rm B}\rangle$ (see Section 6 for the definitions). A rough approximation for $r_{\rm SF}$ is given by the auto-correlation scale of DM haloes of mass $\gtrsim M_h^{\rm min}$. Since $M_h^{\rm min} \geq 10^{2.5} M_{\rm res}$, the quantity can be considered almost independent from resolution (Reed et al. 2009; Guo & White 2014). On the other hand, $\langle R_{\rm B}\rangle$ can be estimated using the Sedov–Taylor approximation (equation 8) with $\langle R_{\rm B}\rangle \propto \langle(\eta_{\rm sn} M_*)^{1/5}\rangle$, where M_* is the stellar mass per halo of mass $M_{\rm h}$. The total stellar mass is calibrated with observations (see Fig. 1) and for $z \lesssim 6$, in each halo with $M_{\rm h} \gtrsim 10 M_h^{\rm min}$, the stellar mass is dominated by PopII (see Fig. 4). Thus, $\langle R_B\rangle$ is expected to be weakly resolution dependent as $\langle R_{\rm B}\rangle \propto (\eta_{\rm sn})^{1/5}$.

As a corollary, when in a simulation $\langle R_{\rm B}\rangle$ becomes comparable with the box size, chemical feedback might be artificially enhanced. However, a robust test of this idea would involve a simulation suite with increasing box size and fixed resolution and a convergence study with fixed box-size and increasing mass resolution. While this is outside the purpose of this work, it would be interesting to analyse the problem in the future.

As a final note, in this paper, we have assumed the same t_* for PopIII and PopII. Considering two distinct star formation time-scales would introduce an extra degree of freedom in the model. The natural way to fix the introduced PopIII time-scale would be fitting cosmic $\rm SFR_{PopIII}$ observations; however, these are not currently available.

APPENDIX B: STRUCTURE IDENTIFICATION

In the present simulation structure, identification is achieved in post-processing via an FOF algorithm (e.g. Davis et al. 1985). While the FOF is readily able to identify particle groups, the method must be modified when dealing with cell-based structure, such as the baryons of RAMSES.

In the simulation, DM and stars are traced by particles. Considering them altogether, the FOF is able to construct the complete halo catalogue and the stellar content associated with each DM group. It is important to highlight that the chosen FOF linking length is calculated by accounting only DM particles. Note that in principle the DM–stellar association can be achieved first by founding with the FOF the DM halo catalogue, then associate each star to a particular halo if the relative distance[9] is less then the halo virial radius.

Additionally, in the simulation, we have identified baryonic groups, such as star-forming regions ($\Delta > \Delta_{\rm th}$) and metal bubbles ($Z > Z_{\rm th} \equiv 10^{-7}\,{\rm Z}_\odot$). This is achieved by slightly changing the FOF algorithm to let it operate on cells rather then particles. First, from the whole baryons we extract only those cells satisfying the relevant threshold criterion, i.e. density based for star-forming regions or metallicity based for bubbles. Then, we let the FOF link the baryons by treating them as particles. It is important to state that the FOF linking length is equal to half the coarse grid size of

[9] Distances are calculated by properly accounting for the periodic boundary conditions of the box.

the simulation. This choice allows the reconstruction of the proper catalogue of structure, but deny substructure identification.

To describe the properties of the baryonic regions found, we can adopt definitions similar to the one used to characterize DM haloes (e.g. Springel, White & Hernquist 2004; de Souza et al. 2013a). The position of a region is given by the location of the density peak, while its 'radius' is defined as $R \equiv V^{1/3}$, where V is the volume occupied by the selected region. As the baryons are extracted from an AMR code, there is no ambiguity in the volume definition. The shape can be described in terms of the eigenvalues I_i of the inertia tensor, where $I_1 \geq I_2 \geq I_3$. The ratios of the principal axis are used as index of sphericity (I_3/I_1), prolateness (I_3/I_2) and oblateness (I_2/I_1). The other physical quantities, such as the temperature $T_{\rm SF}$ and metallicity $Z_{\rm SF}$, are calculated as mass-weighted mean on the cells.

The method for baryon groups identification have been tested on metal bubbles. We have constructed the metal bubble catalogue at various redshifts and for different values of the metallicity threshold, $Z_{\rm th}$. We have checked that the total volume occupied by the identified bubbles gives a filling factor equal to $Q(Z_{\rm th})$ at the selected redshifts (see Fig. 2).

Throughout the paper, we have associated DM haloes and stars with baryonic regions. This is achieved using a distance-based criterion. Each baryonic region is linked with every DM haloes whose position of the centre of mass is inside the boundary of the region. We indicate with $N_{\rm h}$ the number of DM haloes associated with each region. Broadly speaking, for metal bubbles, $N_{\rm h}$ can be regarded as an index indicating degree of merging experienced during the evolution.

APPENDIX C: RENDERING TECHNIQUE

Rendering is an efficient and widely used support tool for a cosmological simulation, since it allows an immediate visual qualitative representation of the data. A large amount of 3D volume rendering algorithms are already present and have been specifically implemented for SPH (Price 2007; Dolag et al. 2008), AMR (Turk & Smith 2011; Labadens et al. 2012b) and moving mesh (Vogelsberger et al. 2013) cosmological codes.

The majority of the available methods are based on a raycasting approach, which is best suited to create images from data obtained from simulations with SPH-type data structure. For this paper, we implement a rendering technique aimed at exploiting the intrinsic AMR nature of the data structure. As a matter of fact, the presence of refinement levels naturally allows the generation of high-definition images. The method is based on a voxel representation, and currently the code is still under development.

Let $\boldsymbol{u}$ denote the bidimensional coordinate of the image to be created and $\boldsymbol{x}$ the spatial coordinate of the data to be rendered. Let $\hat{n}$ denote the direction of the l.o.s. of the observer. As the data is made of AMR cubic cells (e.g. Labadens et al. 2012a,b), the projection $\boldsymbol{u}(\boldsymbol{x})$ from the real space to the image plane depends both on the cell position, orientation respect to $\hat{n}$ and the field of view of the observer. Note that the image resolution is taken to be equal to the finest level of refinement resolved in the simulation; this implies that $\boldsymbol{u}(\boldsymbol{x})$ depends on the size of the cell.

The basic idea is that the cells can be rendered similarly to the marching cube technique (i.e. William & Harvey 1987), thus, in principle, the part of the projection matrix depending on relative orientations can be calculated a priori. Although for now, the algorithm allows only fixed $\hat{n}$ face-on oriented respect to the cells.

To calculate the intensity I of the image, we make use of a back-to-front emission-absorption rendering (e.g. Kähler et al. 2006). After sorting the data by $\hat{n}$, at every pixel I is updated via a transfer like equation

$$\mathrm{d}I\,(\boldsymbol{u}) = (E_{\rm rt}(\boldsymbol{u}(\boldsymbol{x})) - A_{\rm rt}(\boldsymbol{u}(\boldsymbol{x}))I\,(\boldsymbol{u}))\,\rho(\boldsymbol{u}(\boldsymbol{x}))\mathrm{d}n, \tag{C1}$$

where $E_{\rm rt}$ and $A_{\rm rt}$ are, respectively, the emission and absorption coefficients, while ρ is the density field. Like in Dolag et al. (2008), we set $E_{\rm rt} = A_{\rm rt}$ in order to obtain appealing images without artefact effects. We let the coefficient dependents of the characteristic of the cell at $\boldsymbol{x}$ by selecting generalized isosurface, in order to have a smoother and less noisy final image. The rendering of the physical field q is calculated by selecting $i = 1, \ldots, n$ isosurface implicitly defined by calculating the emission coefficient as

$$E_{\rm rt}\,(\boldsymbol{x}) \propto \max_i \left\{ \exp\left[K\left(\frac{q\,(\boldsymbol{x}) - c_i}{h_i} \right) \right] \right\}, \tag{C2}$$

where K is a kernel smoothing function, h_i the bandwidth and c_i the centre of the ith isosurface. The normalization for $E_{\rm rt}$ is chosen in order to avoid I saturation. By using different kernels and varying the isosurfaces, it is possible to obtain different visual effects, which can be best suited for the rendering of different physical quantities.

In particular, Fig. 6 is calculated by choosing six temperature isosurfaces. These are defined by a B-spline kernel function, with centres c_i equispaced in log T, with constant bandwidths satisfying $c_i - c_{i-1} = h_i$. The balancing in the level selection ensure a good dynamical range for the temperature, thus the output is a visual appealing image that gives a representation of the temperature field convolved with the density structure. Note that the convolution is obtained by definition, since in equation (C1) the density has the role of an optical depth.

As said the image resolution taken is linked to the finest level of refinement resolved in the simulation. This oversampling of the image (e.g. Crow 1977) avoids most of the aliasing problems that occurs in rendering a 3D-voxel mesh. On the other hand, the technique augment the image processing time (e.g. Labadens et al. 2012b). However, since the imaging algorithm can be massively parallelized, this does not represent a relevant issue.

Note that it is possible to have additional antialias by directly smoothing the image pixels with their neighbours (Vogelsberger et al. 2013) or – equivalently – by convolving the final image with a proper filter (Labadens et al. 2012b). However, these techniques degrade the image resolution and should not be required after the full implementation of the projection method.

This paper has been typeset from a TEX/LATEX file prepared by the author.